UNIVERSITÀ DEGLI STUDI DI PALERMO

DEPARTMENT OF **E**NERGY, **I**NFORMATION ENGINEERING,
MATHEMATICAL **M**ODELS (D.E.I.M.)

PH.D. in: **Electric, Electronic and Telecommunication Engineering, Mathematics and Automation**

SPECIALISM in: **Mathematics and Automation for Scientific and Technological Innovation**

S.S.D. ING-INF/04

Diagnostic of Supercapacitors based on State Estimation by Extended Kalman Filter

Ph.D.Candidate
Eng. Giulio Rodonò

Ph.D. Course Coordinator
Prof. Maria Stella Mongiovì
UNIPA (Italy)

Tutor
Prof. Eng. Francesco Alonge
UNIPA (Italy)

Co-Tutors
Prof. Eng. Maurizio Cirrincione
UTBM (France) & USP (Fiji)

Prof. Eng. Gianpaolo Vitale,
CNR-ISSIA UOS di Palermo (Italy)

P h D

XXVI CYCLE OF STUDY - YEAR 2016

To my dear family

… der bestirnte Himmel über mir und das moralische Gesetz in mir …

– Immanuel Kant

Acknowledgments

I would like to express my special appreciation and thanks to my advisor Prof. Eng. Francesco Alonge, who has been a guide in studies, in work, in life.

I would also like to really thank my co-tutor Prof. Eng. Maurizio Cirrincione for great support demonstrated, in studies and in welcoming me abroad!

It's important for me to do thank my co-tutor Eng. Gianpaolo Vitale, for his essential and continuous contribute to my PhD work. Also thanks to Giuseppe Santo Scordato and Antonio Sauro, for their precious effort in the set-up of the experimental rig.

A special thank goes to Adriano Fagiolini and Marco Massaro, for their invaluable help.

An huge thank is to my family, for the continuous support and patience and with whom I shared – and continue sharing – joys and sorrows.

How to forget my friends, my dear friends, who had been always close to me and to whom I over-please for the irreplaceable friendship.

Summary

Acknowledgments....5
Summary....7
List of Figures....9
Preface....11
1 Supercapacitor....13
1.1 Capacitor Classification....13
1.2 Supercapacitors Classification....24
1.3 Materials of Supercapacitors....26
1.4 Physical Models....28
1.5 Aging tests of supercapacitors....36
1.5 Common Uses....38
1.6 Benefits and Disadvantages....40
1.7 Nonlinearity Problem and Thesis Goal....42
2 Observability Property....45
2.1 Model of the 2-branch Model....46
2.2 Observability of the SC model....49
2.3 Parametric Analysis....55
3 State Estimation by means of Extended Kalman Filter....59
3.1 Extended Kalman Filter....60
3.2 Designing the Extended Kalman Filter....63
3.3 Simulation results....66
4 Experimental verification of the EKF performance....71
4.1 The experimental set up....71
4.2 Experimental results....76
4.3 Final remarks....103
Conclusions....105
References....107

List of Figures

Figure 1.1 – Schematic representation of a parallel plates and of a cylinder capacitor.....14
Figure 1.2 – Double layer supercapacitor.....15
Figure 1.3 – Schematic representation of a supercapacitor with related materials.....17
Figure 1.4 – Energy Density VS Power Density.....18
Figure 1.5 – Capacitance varies with the frequency.....20
Figure 1.6 – Ragone Chart for batteries and Supercapacitors.....21
Figure 1.7 - An electrolytic battery, for automotive use.....22
Figure 1.8 – Rechargeable batteries, for use in high power electronics.....23
Figure 1.9 – A fuel cell.....24
Figure 1.10 – A *SC*s classification.....25
Figure 1.11 – A classical capacitor.....29
Figure 1.12 – The model of a classical capacitor.....29
Figure 1.13 – SC structure.....30
Figure 1.14 – SCs are made by several thin folis.....30
Figure 1.15 – A model of a supercapacitor.....33
Figure 1.16 – A simplified 3-branch SC model circuit.....35
Figure 1.17 – A simplified 2-branch SC model circuit.....36
Figure 1.18 – Testing the energy efficiency of a bank of four supercapacitors.....38
Figure 2.1 – Schematics of a DLC equivalent circuit.....46
Figure 2.2 – A generic parabola and some characteristic points.....53
Figure 2.3 – Characteristic parabolas defining the observability region.....53
Figure 2.4 – Zoom of the parabolas, near to the point P_2 of the state plane.....54
Figure 2.5 – Zoom of the parabolas, near to the origin of the state plane.....55
Fig. 2.5 – Dependence of the observability region from R_1.....56
Fig. 3.1 – Experimental input-output data.....65
Fig. 3.2. – Output tracking error, with Q=diag(0.0431,0.02155) and R=0.022.....66
Fig. 3.3 – Waveform of the input current used for simulation.....67
Fig. 3.4 – Response of the SC-EKF system; estimation error $e_{x1} = x_1 - z_1$.....68
Fig. 3.5 – Response of the SC-EKF system; estimation error $e_{x2} = x_2 - z_2$.....69
Figure 4.1 – Laboratory Setup.....72
Figure 4.2 – The supercapacitor module.....74
Figure 4.3 – SC-Toolbox, part I.....75
Figure 4.3 – SC-Toolbox, part II.....75
Fig 4.4a – Estimation of $\hat{x}_1$ and $\hat{x}_{1,w}$, with $I_d = \pm 5A$.....80
Fig. 4.4b – Estimation of $\hat{x}_2$ and $\hat{x}_{2,w}$, with $I_d = \pm 5A$.....81
Fig 4.5a – Estimation of $\hat{x}_1$ and $\hat{x}_{1,w}$, with $I_d = \pm 10A$.....83
Fig 4.5b – Estimation of $\hat{x}_2$ and $\hat{x}_{2,w}$, with $I_d = \pm 10A$.....84
Fig. 4.6a – Estimation of $\hat{x}_1$ and $\hat{x}_{1,w}$, with $I_d = \pm 15A$.....86
Fig 4.6b – Estimation of $\hat{x}_2$ and $\hat{x}_{2,w}$, with $I_d = \pm 15A$.....87
Fig 4.7a – Estimation of $\hat{x}_1$ and $\hat{x}_{1,w}$, with $I_d = \pm 20A$.....89
Fig. 4.7b – Estimation of $\hat{x}_2$ and $\hat{x}_{2,w}$, with $I_d = \pm 20A$.....90
Fig 4.8a – Estimation of $\hat{x}_1$ and $\hat{x}_{1,w}$, with $I_d = \pm 25A$.....92
Fig 4.8b – Estimation of $\hat{x}_2$ and $\hat{x}_{2,w}$, with $I_d = \pm 25A$.....93
Fig. 4.9a – Estimation of $\hat{x}_1$ and $\hat{x}_{1,w}$, with $I_d = \pm 30A$.....95

Fig. 4.9b – Estimation of $\hat{x}_2$ and $\hat{x}_{2,w}$, with $I_d = \pm 30A$ 96
Fig. 4.10a – Estimation of $\hat{x}_1$ and $\hat{x}_{1,w}$, with $I_d = \pm 35A$ 98
Fig. 4.10b – Estimation of $\hat{x}_2$ and $\hat{x}_{2,w}$, with $I_d = \pm 35A$ 99
Fig. 4.11a – Estimation of $\hat{x}_1$ and $\hat{x}_{1,w}$, with $I_d = \pm 40A$ 101
Fig 4.11b – Estimation of $\hat{x}_2$ and $\hat{x}_{2,w}$, with $I_d = \pm 40A$ 102

Preface

Since the dawn of time, energy has been the keystone of evolution and it allowed to create human society as we see it today. As History teaches, first steps were time-consuming. Depending on the historical periods, discoveries were accepted and used or rejected being considered too revolutionary, or even against human thinking and nature. During XVIII century something changed: there was a general betterment in arts, in philosophy, in politics and also in technology. Afterwards, during XIX century, with the Industrial Revolution there was a technological soaring in Europe and North America. During XX-XIX centuries, energy request has increased and did also produce pollution. During last decades, due to the global crisis and thanks to a better consciousness, energy saving is a present and serious problem for globalindustry. And so, for mankind.

During the past, we found several ways to solve how to use energy sources (muscular, water flows, steam, petrol, nuclear, etc...) and how to transport them (railways for coal, electric networks for electricity, etc...). Several solutions have been studied and used for saving goods, such as refrigerators for food and batteries for electric saving. These have a long history of evolution and use; currently, mostly used types are those based on lead and acid (stored chemical energy is converted into electrical one, i.e. cars) and those on lithium (mostly used in low power devices, such as mobiles).

Today, the conscious use of energy allows a greater efficiency of the devices, while storage permits to use (and reuse) energy only when necessary. Moreover,

several renewable energies are used today. A serious still present problem is electric storage, partially solved with batteries. A possible solution is given by the so-called \supercapacitors ", which offer great energy density and often work complementing batteries. A supercapacitor, for its intrinsic double-layer technology, is usually called as \SC" or \DLC " or \EDLC " , scilicet (respectively) \Super-Capacitor", or \Double-Layer Capacitor", or \Electric Double-Layer Capacitor".

The goal of this Thesis is an electronic system, with a supercapacitor, for storing electric energy. Together with theoretical study, simulations and laboratory results are present. The Thesis has been carried out during the PhD course, which lasted three years. It is also the result of two papers, of which I have been the Author (the first paper in published, the second one is accepted at the 16 IEEE).

- "Observability of a 2-branch Double-Layer-Capacitor" - F. Alonge, M. Cirrincione, G. Vitale, G. Rodonò - Renewable Energy and Power, Quality Journal (RE&PQJ) ISSN 2172-038 X, No.13, April 2015 (see:http://www.icrepq.com/icrepq'15/403-15-alonge.pdf)
- “An EKF for State Estimation of a Supercapacitor Model, for Diagnostic Purpose” accepted for presentation at the 16 IEEE International Conference on Environment and Electrical Engineering, special session on Monitoring, diagnosis and reliability of renewable energy sources and electric vehicles, FLORENCE, ITALY, 7-10 JUNE, 2016

1 Supercapacitor

Nowadays, the need of electrical storage is increasingly important. There are many devices able to store electrical energy, which offer many features in terms of capacity, charge time, delivery, working power. In the market, therefore, there are many types of electric accumulators.

1.1 Capacitor Classification

The electrochemical double layer capacitors are able to meet several requirements in various fields of the electronics. The first applications were born in the 70's as back-up systems for computers, already under the name of supercapacitors. In the 90's there were the first applications of high-power supercapacitor, for military use and for electric vehicles.

The traditional capacitors accumulate energy in the form of electrostatic charges on the two conductors (electrodes) separated by a dielectric. The capacitance is known to be provided by the formula

$$C_b = k\, v \tag{1.1}$$

where: C is the capacitance in Farads, Q is the accumulated charge in Coulomb, the voltage V in volts, ε is the constant dielectric, A is the surface of the electrode, D is the distance between the two electrodes. For a cylinder capacitor the capacity is given by:

$$C = 2\pi\varepsilon_0\varepsilon_r \frac{l}{\ln\left(\frac{r_1}{r_2}\right)} \tag{1.2}$$

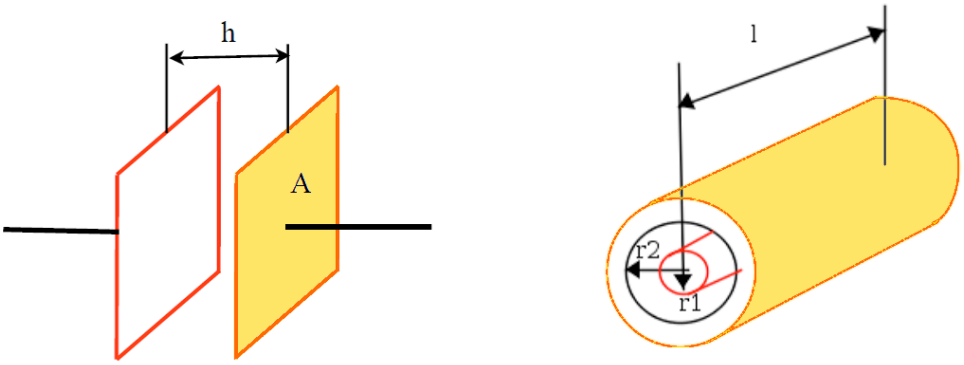

Figure 1.1 – Schematic representation of a parallel plates and of a cylinder capacitor.

The stored energy U is given by:

$$U = \frac{1}{2}CV^2 = \frac{1}{2}QV \tag{1.3}$$

It can be noted that the higher the capacitance value and the voltage at the capacitance terminals the higher is the stored energy. The capacitance contribution can be increased by a large surface as in the cylinder assembly.

In a double-layer capacitor, the charges (accumulated in the separation surface between the electrode and electrolyte) form two layers of opposite charge. If the electrodes are of the type with a large surface area, it is possible to reach an

electrostatic capacity much higher than one in the traditional condensers, at equal volumes and weights involved. The fundamental model, proposed by Helmholtz in 1853, is based on the assumption of the presence of a single layer ion, on the electrode surface. The differential capacitance is given by:

$$C_1 = A\varepsilon / 4\pi\delta \tag{1.4}$$

where δ indicating the distance between the center of the layer ion and the electrode. This first model provides a consistent ability and does not take into account the dependence of the same capacity and the voltage on the ion concentration.

Helmotz developed the theory of the electrical double layer; it can be considered as a structure composed of two electrodes plunged in an electrolytic solution. This forms an electrochemical cell in which the two electrodes contribute twice to the charge transfer. The former for the positive ions and the latter for the negative ions. The theory of the electrical double layer can be sketched with two series connected capacitors as in figure 1.2.

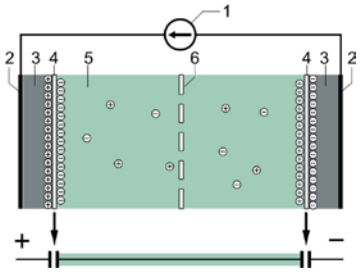

Figure 1.2 – Double layer supercapacitor.

1) generator – 2) electric terminals – 3) electrods
4) reaction surface – 5) electrolyte – 6) separator.

The model of Gouy Chapman, however, supposes that the charge is present in a diffused layer. The formula then becomes:

$$C_2 = \frac{\varepsilon K \cosh(z/2)}{4\pi} \tag{1.5}$$

where z is the valence of the ions, k is the reciprocal of the length of Debye-Huckel. Finally, Stern concluded that the total capacity were:

$$\frac{1}{C} = \frac{1}{C_1} + \frac{1}{C_2} \tag{1.6}$$

The material far more used for the electrodes is carbon, which has the following advantages: low cost, easy availability, long-lasting use. It is important that the carbon electrodes are provided with a diffuse porosity of appropriate dimensions, in order to have a wide contact surface with the electrolyte, easily accessible for ions.

The voltage reached from a supercapacitor is limited by the tensile strength of its electrolyte, which can be organic or in aqueous solution (see Fig.1.1.)

The organic electrolyte allows reaching voltages of the order of 2 V, but it has an high resistance to the passage of the current. The aqueous electrolyte does not allow to overcome tensions around 1 V (variable depending on the composition of the electrolyte itself), but it has a lower resistance and it is cheaper. The choice of the electrolyte and the electrodes is interdependent, because the electrolyte determines the type, size and mobility of the ions, characteristics that interfere with the size and the surface of the pores of the electrodes. The most important cause of

energy dissipation in a supercapacitor is provided by the internal resistance, which includes the resistances of the various components, flowed through by current. In a simple equivalent circuit, you can draw an ideal capacitor connected in series with a resistance, sum of different contributions. The principle of operation of the supercapacitor is based on the mobility of the ions in the pores of the electrodes.

Usually the electrodes are made by Aluminium, they are covered by active carbon or carbon nanotubes to increase the contact surface. A separator is plugged inside the electrolyte, it does not cause a short circuit between the electrodes but allows the transfer of the ions.

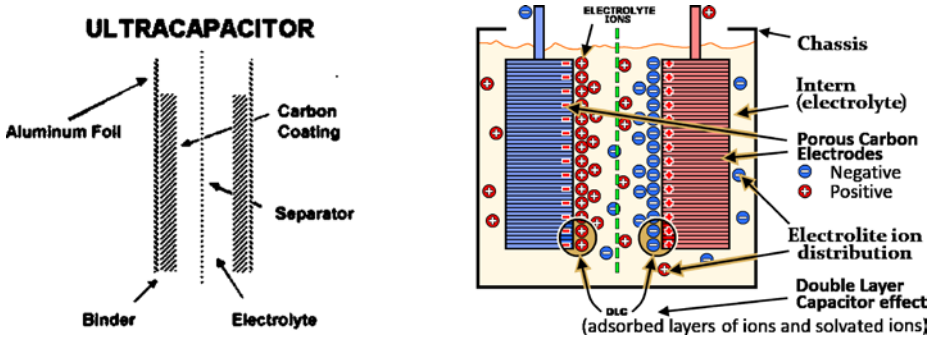

Figure 1.3 – Schematic representation of a supercapacitor with related materials.

Actually up-to-date supercapacitors electrodes exhibit a very low resistance and a wide contact surface thanks to carbon nanotubes technology. In this way it is possible to obtain a cylinder with 2.2 nm of diameter. On the other hand the use of this material causes an impedance variation with frequency.

As for the electrolytes, there are compounds as H_2SO_4KOH with high conductivity (up to 1 S/m) but low voltage (lower than 1 V) or, alternatively, organic electrolytes $C_2H_5)_4NBF_4$ that exhibit higher voltage (up to 3.5 V) but a lower conductivity (about 1.5 10^{-2} S/cm).

Two main separators can be recognizable. The former are made by polymers and cellulose fiber and the latter are ceramic or glass fiber separators.

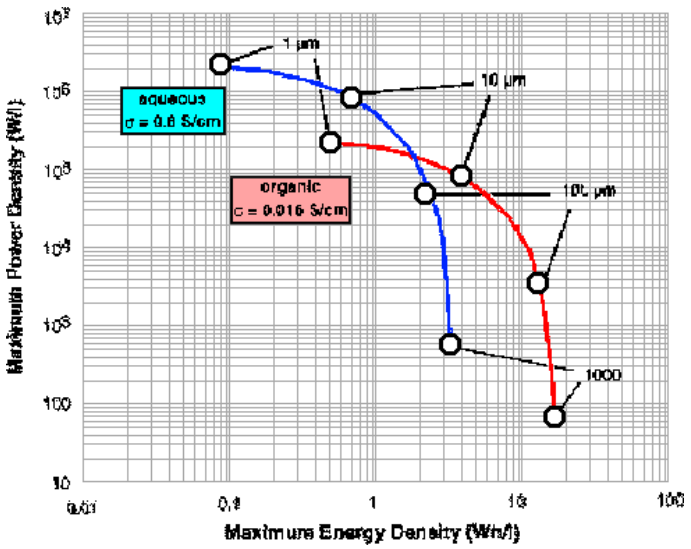

Figure 1.4 – Energy Density VS Power Density.

The capacitance decreases as frequency (and speed) increases with the ion motion (as in Fig. 1.5).

Supercapacitors are much more effective of electrochemical batteries, because of they instantaneously provide high powers, but are not able to accumulate as much energy. Using them in parallel with electrochemical batteries allows dividing the tasks optimally: batteries

store energy, while supercapacitors provide the power peaks. The presence of super capacitors also reduces the stress to the batteries due to current spikes.

A supercapacitor can be characterized by its efficiency defined as the ratio of the energy delivered during the discharge phase and the supplied energy.

$$\eta_e = \frac{E_{dch}}{E_{ch}} = \frac{\int_{in}^{fin} v_{dch}(t) \cdot i_{dch}(t)\,dt}{\int_{in}^{fin} v_{ch}(t) \cdot i_{ch}(t)\,dt} \tag{1.7}$$

The supercapacitor efficiency can be described by its internal resistance defined as the sum of all resistance of its internal components. It is possible to obtain this parameter by measurement as:

$$R_m = \frac{P_{diss}}{I_{rms}^2} = \frac{E_{ch} - E_{dch}}{I_{rms}^2 \cdot T} \tag{1.8}$$

where Irms is the root mean square of the current and T is the duration of the test. Usually the internal resistance is lower than 10 mohm and the efficiency is greater than 90%. It must be remarked that during operation, due to aging, the internal resistance can increase worsening the device performance.

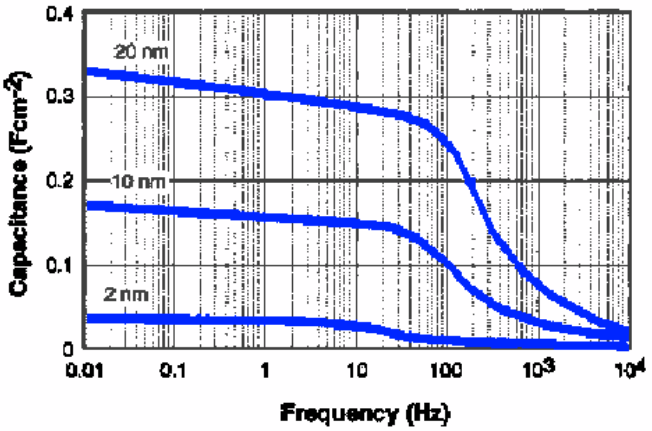

Figure 1.5 – Capacitance varies with the frequency.

In electric vehicles powered by fuel cells, supercapacitors can absorb energy during braking (otherwise dissipated) and provide the energy needed for acceleration. The regenerative braking can lead to save 15%. The design criteria allows choosing the most suitable for the required supercapacitor. Many applications need voltage levels higher than those typical of the supercapacitor. In that case, it is useful to coupling in series a certain number of elements (this involves an increase of the resistance in series; to reduce it, it is possible to connect in parallel several strings of capacitors). To prevent that the sum of the voltage values of internal resistance could reach the maximum permissible voltage, it is necessary a suitable compensation circuit of the voltage.

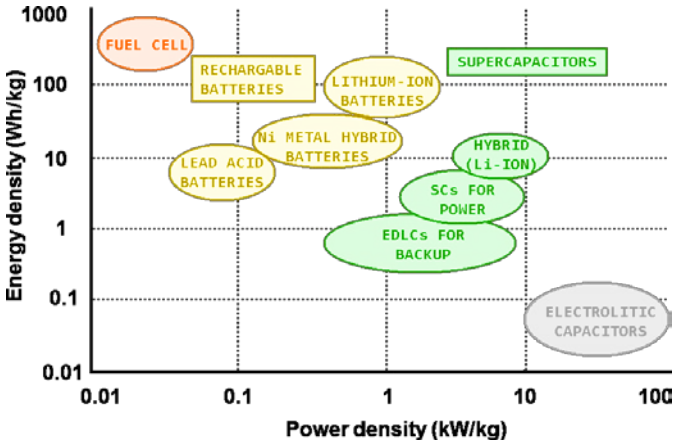

Figure 1.6 – Ragone Chart for batteries and Supercapacitors.

In Fig. 1.6 there is an overview, given by a Ragone Chart [3], which is often used in science to classify and compare the new devices with the old ones. Power density describes the speed at which energy can be delivered to (or absorbed from) the load; the energy density is the amount of energy per volume, that can be stored in a capacitor.

The maximum power density is offered by Electrolytic Capacitors, or E-Caps (see Fig.1.7); they are polarized capacitors that store electrical energy, through a positive terminal (+) and a negative one (-); energy goes into an insulating oxide layer, which acts as the dielectric of the electrolytic capacitor [4]. The oxide layer is very thin and its surface very enlarged, so that power density can be very high. Moreover, the large capacitance makes E-Caps really suitable for passing or bypassing low-frequency signals up to some mega- hertz and storing large amounts of energy. E-Caps are often used– also – for decoupling or noise filtering

in power supplies and DC-link circuits, and their dielectric is really sensible to voltages with reverse polarity, or voltage or ripple current higher than specified.

Figure 1.7 - An electrolytic battery, for automotive use.

Rechargeable Batteries, or *RB*, as in Fig.1.8, are *accumulators* that can be charged, discharged (into a load) and re-charged several times [5]. They are composed of one or more electrochemical cells, in which there is a reversible electrochemical reaction. they are used almost everywhere, from small button battery up to ones for mega-watt electric networks. They are made by several combinations of electrode materials and electrolytes, such as lead–acid, nickel cadmium (NiCd), nickel metal hydride (NiMH), lithium ion (Li-ion), and lithium ion polymer (Li-ion polymer). Although more ex pensive than the non-rechargeable batteries, rechargeable batteries offer a final working costs which is really lower (with respect to non-rechargeable batteries), thanks to the possibility of re-charge them many times. Furthermore, there

is no need to substitute them after a single cycle of charge-discharge and the environmental impact is lower; some times they have the same shape of the non-rechargeable batteries, so the two types are interchangeable.

Figure 1.8 – Rechargeable batteries, for use in high power electronics.

A fuel cell, or *FC*, is a device (see Fig.1.9) that converts the chemical energy – from a fuel – into electricity through a chemical reaction of hydrogen ions (positively charged) with an oxidizing agent [6]. All *FC*s consist of an electrolyte that allows to the positively charged hydrogen ions (or protons) to move between the two sides of the same *FC* (anode and cathode). The reaction gives positively charged hydrogen ions at the cathode (together with electrons and oxygen, they give water and heat) and electrons at the anode (they go from the anode to the cathode through an external circuit, producing direct current electricity). Although *FC*s need of a continuous source of fuel and oxygen or air to sustain the chemical reaction and to generate an electromotive force (emf), they can produce electricity continuously (as long as hydrogen and air are present). After being used by

NASA in aerospace missions, *FC*s had been used in several fields, such as primary and backup power for commercial, industrial and residential buildings, and in *FC* vehicles (as buses, boats, motorcycles, submarines). Main *FC*s classification is made by the type of electrolyte used and by the difference in startup time ranging: from 1 second for proton exchange membrane *FC*s (*PEMFC*), up to 10 minutes for solid oxide *FC*s (*SOFC*). A single *FC* produces relatively small electrical potentials, about $0.7V$; so cells are "stacked" to create sufficient voltage [7] for an application's requirement.

Figure 1.9 – A fuel cell.

1.2 Supercapacitors Classification

Supercapacitors, *SC*s, occupy the gap between high power/low energy electrolytic capacitors and low power/high energy rechargeable batteries. *SC*s, in their turn, are categorized (see Fig. 1.10) by their behaviour [8] and, hence, mainly classifiable in Pseudo-capacitors *PC*s, Double-Layer Capacitors *DLC*s (orElectrical Double-Layer Capacitors *EDLC*s), Hybrid Capacitors *HC*s.

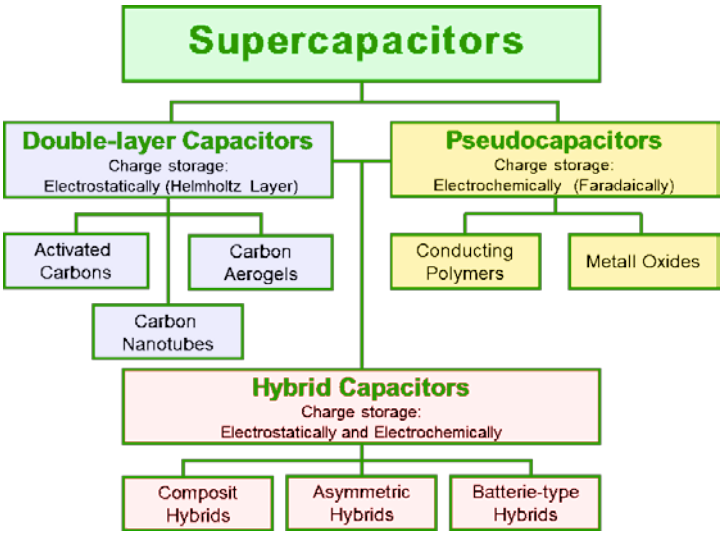

Figure 1.10 – A *SC*s classification.

DLC s use carbon electrodes or derivatives with much higher electrostatic double-layer capacitance than electrochemical pseudo-capacitance, achieving separation of charge in a Helmholtz [9, 10, 11] double layer at the interface between the surface of a conductive electrode and an electrolyte.

Electrical charge storage is stored electrostatically, with no interaction between the electrode and the ions *DLC*s are made of conducting polymers or metaloxides. *EPS*s use metal oxide or conducting polymer electrodes with an high amount of electrochemical *pseudocapacitance*, which is achieved by Faradaic electron charge-transfer (between electrode and electrolyte) with red-ox reactions, intercalation processes or electrosorption [12, 13]. A pseudocapacitance can be higher by a factor of 100 as a double-layer capacitance with the same electrode surface. In add, the redox reactions (charging and discharging) of *SC*s are much faster than ones in batteries. Hybrid capacitors, such as the lithium-ion capacitor, use electrodes

with differing characteristics: one exhibiting mostly electrostatic capacitance and the other mostly electrochemical capacitance. The electrolyte forms a conductive connection between the two electrodes which distinguishes them from electrolytic capacitors where the electrolyte is the second electrode (the cathode).

1.3 Materials of Supercapacitors

In general, *SC*s improve storage density through the use of a nanoporous material, typically activated charcoal, in place of the conventional insulating barrier. Activated charcoal is an extremely porous, spongy form of carbon with an extraordinarily high specific surface area – a common approximation is that 1 gram (a pencil-eraser-sized amount) has a surface area of roughly $250m^2$ – about the size of a tennis court.

Graphene has excellent surface area per unit of gravimetric or volumetric densities, is highly conductive and can now be produced in various labs, but it is not available in production quantities.

Carbon nanotubes have excellent nanoporosity properties, allowing tiny spaces for the polymer to sit in the tube and act as a dielectric. They can store about the same charge as charcoal (which is almost pure carbon) per unit surface area but nanotubes can be arranged in a more regular pattern that exposes greater suitable surface area. The addition of carbon nanotubes in capacitors can

greatly improve and enhance the performance of electric double-layer capacitors.

Carbon aerogel provides extremely high surface area gravimetric densities of about 400–1000 m^2/g. The electrodes of aerogel supercapacitors are acomposite material usually made of non-woven paper made from carbon fibres and coated with organic aerogel, which then undergoes pyrolysis. Mineral- based carbon is a non-activated carbon, synthesized from metal or metalloid carbides; the synthesized nano-structured porous carbon, often called Carbide Derived Carbon (CDC), has a surface area of about 400 m^2/g to 2000 m^2/g with a specific capacitance of up to 100F/mL (in organic electrolyte).

Researchers combined a biodegradable paper battery with aligned carbon nanotubes, designed to function as both a lithium-ion battery and a supercapacitor, called bacitor. The device employed an ionic liquid, essentially a liquid salt, as the electrolyte. The paper sheets can be rolled, twisted, folded, or cut with no loss of integrity or efficiency, or stacked, like ordinary paper (or a voltaic pile), to boost total output. They can be made in a variety of sizes, from postage stamp to broadsheet. Their light weight and low cost make them attractive for portable electronics, aircraft, cars, and toys (such as model aircraft), while their ability to use electrolytes in blood make them potentially useful for medical devices such as pacemakers.

1.4 Physical Models

The study of physical models is really helpful to understand how a device works, in its every parts and behaviors; furthermore, a mathematical model of a device can be a great instrument to apply mathematical and engineering laws, doing simulations, obtain estimation of inaccessible parameters, and so on. Here follow two studies; the firs is referred to "classical" capacitors and their mathematical model. After that, there is a study of the physical and mathematical models of a supercapacitor.

1.4.1 Classical Capacitors

Before speaking about *SC*, it is useful to do a brief resume of a classical capacitor (see Fig. 1.11). As is well known, a capacitor is a passive electrical component able to store energy, in the form of electrostatic energy. Denoting with Q, V and C, respectively, the charge stored, the voltage across its two terminals and the linear capacitance C, the relationship between these quantities is given by $Q = CV$. However, the electric scheme of the capacitor is that shown in Fig. 1.12, where R is a resistance of a convenient value. So, when the capacitor is connected to a source of constant voltage E, the voltage between its terminals increases and tends towards E with a time constant $\tau = RC$.

Figure 1.11 – A classical capacitor.

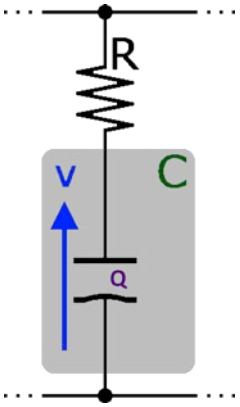

Figure 1.12 – The model of a classical capacitor.

1.4.2 Supercapacitors Physics

A different discourse, now, is needed for a *supercapacitor*, *SC*, which is a nonlinear capacitor. Rather than two plates [12] separated by an intervening insulator (as in conventional capacitors), a *SC* uses virtual plates that are *de facto* two layers of the same substrate, realizing the phenomenon of the so-called Helmholtz [13] "electrical double layer" (see Fig. 1.13). It results in the

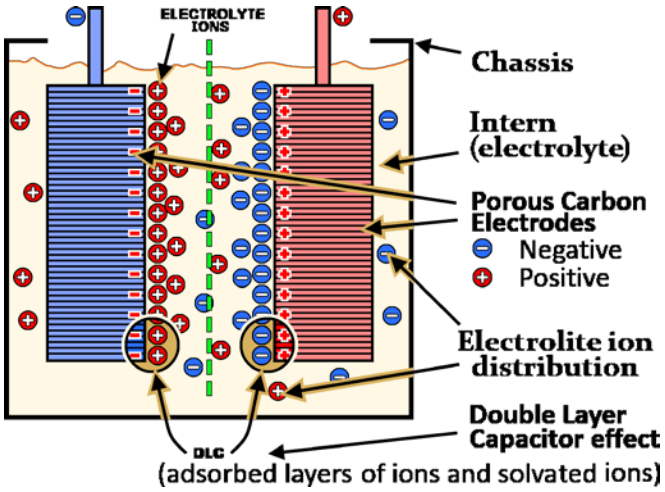

Figure 1.13 – SC structure

effective separation of charge despite the infinitely thin (some nanometres) physical separation of the layers (*SC*s are mainly made from polymer foils (as in Fig. 1.14).

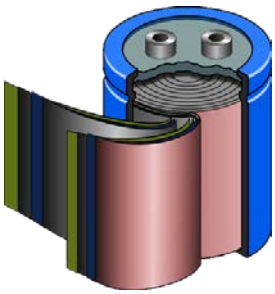

Figure 1.14 – SCs are made by several thin folis.

The absence of need of a great layer of dielectric, and the porosity of the material used (most used one is activated carbon [14]), permits

the packing of plates with much larger surface area into a given volume, resulting in high capacitances in practical-sized packages.

In an electrical double layer, each layer by itself is quite conductive, but the physics at the interface where the layers are effectively in contact means that no significant current can flow between the layers. The double layer can tolerate only a low voltage – maximum is $3V$ – which means that electric double-layer capacitors rated for higher voltages must be made of matched series-connected individual SCs, much like series-connected cells in higher-voltage batteries.

*SC*s have much higher power density [12] than batteries. Power density combines the energy density with the speed at which the energy can be delivered to the load. Existing *SC*s have energy densities that are perhaps 1/10 than ones of a conventional battery, their power density is generally 10 to 100 times as great. This makes them most suited to an intermediary role between electrochemical batteries and electrostatic capacitors. As already said, *SC*s are commercially and technologically attractive because they havea higher power density than batteries, do not need special charging circuitry, and have a long operational lifetime; the number of charge/discharge cycles usually considered to be unrelated [15] to the number of charge/discharge cycles. The dielectric of *SC*s consists of an electrolyte sandwiched between two electrolytic areas of high porosity (and therefore high specific surface area). Voltage applied to the *SC* terminals determines the formation of a very thin double layer in correspondence of each of the two electrode–electrolyte interfaces. The unitary capacitance

of these devices is very high. On the contrary, the voltage supply is low (maximum 3 V), having an upper limit which is equal to the solvent decomposition potential. An equivalent theoretical model can be obtained from a complicated network of resistor and voltage-dependent non-linear capacitor branches, connected in parallel by resistors. The values of the resistances to insert in the equivalent circuit depend on several parameters, such as: the resistance of the electrode materials – the resistance of the electrolyte – pores sizes – membrane porosity – the quality of the electrode-collector contacts.

These parameters bring to a very complicated model; hence, in this Thesis, a simplified physic model is presented.

1.4.3 Supercapacitor Physical Model

In the literature, some studies assume the behavior of the supercapacitors as either ideal devices [16], or simplistic models explaining their short-term behaviour [16]. A more accredited circuital model is the ladder one [1, 17], which uses a ladder of resistors and capacitors, i.e. a circuit of n branches consisting of the parallel connections of n groups R-C series connected; the first one contains a series connection of a resistance and a nonlinear capacitance depending of the voltage at its terminals, and the remaining (n-1) groups consist of linear resistance and capacitance. In and the one proposed in [18, 19] the circuital model is simplified assuming n=3, and the components

appearing in the circuit are justified considering the input-output behavior of the supercapacitor. In particular, each branch represents a behavior of the SC in a specific working time. This is possible assuming each branch to operate independently from the other ones. Another model used frequently is that employing two branches, derived also from the input-output behavior of the SC.

In both cases, i.e. two or three branches, the first branch displays the circuital scheme of Fig. 1.15. The resistance *R* is series connected to the parallel of a linear capacitance and a nonlinear capacitance proportional to the voltage at its terminals.

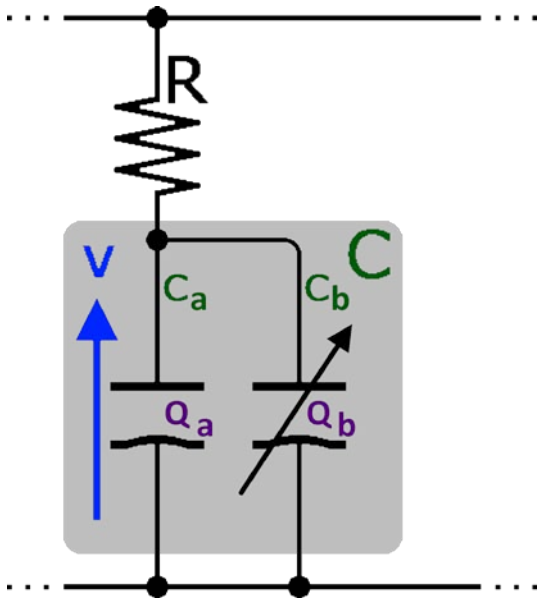

Figure 1.15 – A model of a supercapacitor.

In the literature there exist several equations which that describe the functional relationship for C_b [20]. In this Thesis, C_b is given by the equation (cf. [1]):

$$C_b = k \quad v \tag{1.9}$$

where k is a constant and v is the voltage across C . Hence, the equation for C is:

$$\begin{aligned} C &= C_a + C_b = \\ &= C_a + kv \end{aligned} \tag{1.10}$$

However, in order to obtain the dynamical model of the system that contains the component in question, the differential capacitance C_{diff} is involved. This capacitance is defined as follows (cf. [18]):

$$C_{diff} = \left.\frac{dq}{dv}\right|_v \tag{1.11}$$

where dv is the incremental capacitor voltage, and dq is the corresponding incremental change in the stored charge at a certain capacitor voltage v that produces dv . From the scheme of Fig. 1.10, we have:

$$q = q_a + q_b = (C_a + kv)v \tag{1.12}$$

and consequently:

$$C_{diff} = (C_a + 2kv) \tag{0.13}$$

SC 3-branch physical Model

The 3-branch physical model is shown in Fig. 1.16. It presents the first branch as in Fig. 1.15, whereas the second and third branch consist simply of two RC groups series connected, with R and C constant. This

physical model offers a better modelling, which takes into account also long working times operations.

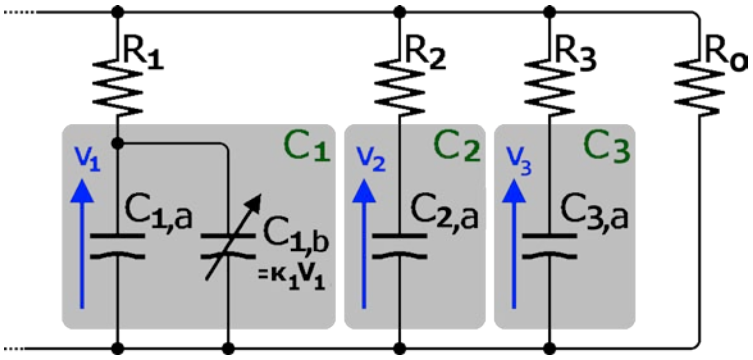

Figure 1.16 – A simplified 3-branch SC model circuit.

SC 2-branch Model

The 2-branch model, shown in Fig. 1.17, was introduced in [1, 2]. It is quite simpler, but good enough to reproduce the *SC* behavior. In [1] a method is proposed for determining the parameters of the circuit of Fig. 1.17. In the present thesis, this 2-branche physical model will be considered for successive developments.

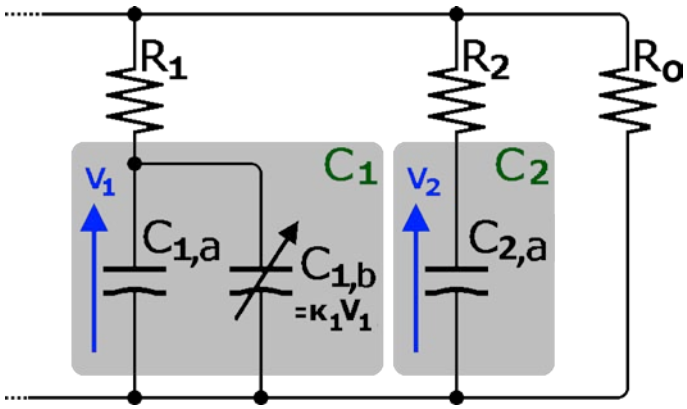

Figure 1.17 – A simplified 2-branch SC model circuit.

For both of the above physical models, the parameters have to be obtained and this is carried out following, for example the procedure described in [1] and [2].

1.5 Aging tests of supercapacitors

To carry out tests of aging of supercapacitors, reference quantities are defined, as magnitudes that at a distance of periods of time, through the measurements, are calculated and compared to the reference, making it possible to obtain the aging of the capacitor. They are measured in test benches, where one or more supercapacitors in series with the balance circuits are subjected to voltages and currents of charge and discharge to obtain the desired sizes. The parameters that allow the analysis of aging of a supercapacitor are: Faradic capacity, energy performance, internal resistance.

The Faradic capacity represents the amount of charge stored by a capacitor in relationship to the voltage applied at its terminals, and can be calculated or calculating the change of energy stored in the component in relation to a discharge voltage, or by measuring the amount of charge delivered in relation with the discharge voltage).

The energy performance is the ratio between the charge energy and the discharge energy and, thus, the losses of energy that the different resistances - within the component - dissipate into heat. To calculate the energy performance of the component, several cycles of charge and discharge have been done, at constant current and of the same form. As in Fig. 1.18, the phases of charging and discharging are spaced by a time t of 10 s to allow the voltage to stabilize within the supercapacitor. This test is repeated for different values of current and begins and ends with a phase of the total charge of the component, for having within it the same value nominal energy.

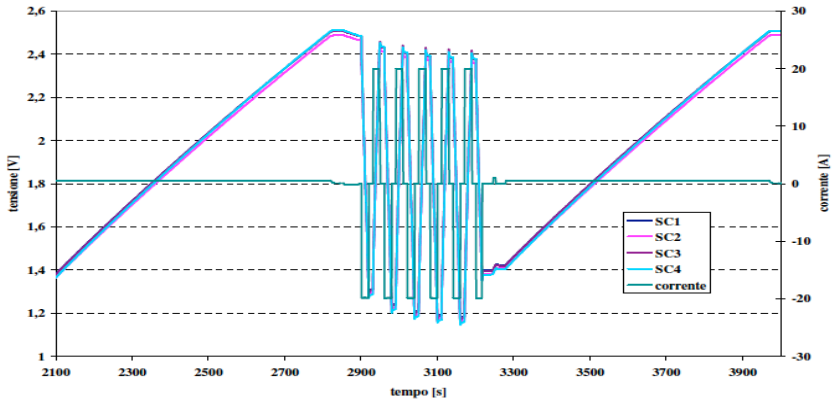

Figure 1.18 – Testing the energy efficiency of a bank of four supercapacitors.

The internal resistance is the sum of all the resistances that compose the elements of the supercapacitor. The measurement of the parameters - useful to test internal resistance - are obtained from the acquisition, that is made on the component in the test for the energy performance of the SC : during the several cycles, if the voltages - and so the capacitances- will result lower than ones estimated during first cycles (when the SC is almost new), then a usury status can be deduced. When this status will be lower than the one which permits a good functionality of the SC , there will be the necessity of substitute the SC itself.

1.5 Common Uses

Supercapacitors are used in some concept prototype vehicles, in order to keep batteries within resistive heating limits and extend battery

life. The “ultra battery” combines a supercapacitor and a battery in one unit, creating an electric vehicle battery that lasts longer, costs less and is more powerful than current plug-in hybrid electric vehicles.

It was proposed, for *Formula 1*, that a new set of power train regulations can be issued including a hybrid drive of up to 200 kW input and output power using “superbatteries” made with both batteries and supercapacitors. Practical example: the *SC* and flywheel energy storage devices, whose rapid charge- discharge capabilities help both in rapid braking and rapid acceleration, made the Audi and Toyota hybrids the fastest cars in the race.

When used in conjunction with rechargeable batteries in uninterruptible power supplies and similar applications, the *SC* can handle short interruptions, requiring the batteries to be used only during long interruptions, reducing the cycling duty and extending their life *SC*s can be used to operate low-power equipment such as PC Cards, photographic flash, flash lights, portable media players, and automated meter reading equipment. They are advantageous when extremely fast charging is required.

1.6 Benefits and Disadvantages

Supercapacitors have lots of benefits, such as a long life, with little degradation over hundreds of thousands of charge cycles. Due to the supercapacitors high number of charge-discharge cycles (millions or more compared to 200 to 1000 for most commercially available rechargeable batteries) it will last for the entire lifetime of most devices, which makes the device environmentally friendly. Rechargeable batteries wear out typically over a few years, and their highly reactive chemical electrolytes present a disposal and safety hazard. Battery lifetime can be optimized by charging only under favorable conditions, at an ideal rate and, for some chemistries, as infrequently as possible. *SC*s can help in conjunction with batteries by acting as a charge conditioner, storing energy from other sources for load balancing purposes and then using any excess energy to charge the batteries at a suitable time. Moreover, *SC*s have the properties of low cost per cycle, a good reversibility, a very high rates of charge and discharge, an extremely low internal resistance (ESR) and consequent high cycle efficiency and extremely low heating levels, an high output power. They presents a specific power of electric double- layer capacitors can exceed 6*kW/kg* at 95% efficiency, an improved safety, no corrosive electrolyte, low toxicity

of materials. Finally, no full-charge detection is needed, there is no danger of overcharging. When used in conjunction with rechargeable batteries, in some applications, the SC can supply energy for a short time, reducing battery cycling duty and extending life. The amount of energy stored per unit weight is generally lower than that of an electrochemical battery (3–5 $W*h/kg$ for a standard ultracapacitor, although 85 $W\,h/kg$ has been achieved in the lab as of 2010 compared to 30–40 $W\,h/kg$ for a lead acid battery, 100-250 $W\,h/Kg$ for a lithium-ion battery and about 0.1% of the volumetric energy density of gasoline. Has the highest dielectric absorption of any type of capacitor. High self-discharge – the rate is considerably higher than that of an electrochemical battery. Low maximum voltage – series connections are needed to obtain higher voltages, and voltage balancing may be required. Unlike practical batteries, the voltage across any capacitor – including *SC*s – drops significantly as it discharges. Effective storage and recovery of energy requires complex electronic control and switching equipment, with consequent energy loss. A detailed paper on a multi-voltage 5.3$W\,SC$ power supply for medical equipment discusses design principles in detail. It uses a total of 55F of capacitance, charges in about 150 seconds, and runs for about 60 seconds. The circuit uses switch-mode voltage regulators followed by linear regulators for clean and stable power, reducing

efficiency to about 70%. About the types of switching regulator available, for the widely varying voltage across an *SC* buck-boost is best, boost second-best, and buck unsuitable. Very low internal resistance allows extremely rapid discharge when shorted, resulting in a spark hazard similar to any other capacitor of similar voltage and capacitance (generally much higher than electrochemical cells).

1.7 Nonlinearity Problem and Thesis Goal

The goal of the present thesis is the setup of a method for carrying out the diagnostics of the functionalities of Supercapacitors. To this regard, the main problem is due to the fact that in the electrical scheme 1.17, the two terminals through which the SC is supplied at a constant current are the unique terminals accessible for measurement. The two voltages v_1 and v_2 cannot be measured. Moreover, the first branch in Fig. 1.17 contains a capacitance driven by the voltage v_1 and, consequently, the mathematical model which can be associated to the circuit of Fig. 1.17 is nonlinear. Finally, a further problem is that relative to the determination of a suitable set of parameters that allows to perform an accurate analysis of the system in which the SC is inserted.

In the follows, the diagnostics of the SC will be carried out starting from a mathematical model of the SC itself. It follows that the first step

is that of obtaining a good set of the parameters which appear in the model of Fig. 1.17. The second step is that of proving the observability property of the SC model. The third step is that of designing a state estimator. Considering that the model of the SC is nonlinear, an Extended Kalman Filter (EKF) is used in order to estimate the two state variables v_1 and v_2 of the model.

During the several cycles of operations, if the voltages, and so the capacitances, will result lower than those estimated during first cycles (when the *SC* is almost new), then a usury status can be deduced. When this status will be lower than that which permits a good functionality of the *SC*, then will be necessary to substitute the *SC* itself.

2 Observability Property

In control theory, the state observer permits to estimate the internal variables of a given system, knowing just its input and the output variables. It is important to notice that if a system is *observable*, it is possible to fully reconstruct its state variables from input and output measurements, by means of the state observer.

For nonlinear systems some observability concepts can be defined [23]. The concept used here is that of local weak observability. In intuitive terms, we can say that a system is locally weakly observable if $\forall x(t_0) = x_0 \in X$, if there exist an open neighbourhood U of x_0 such that the output response corresponding to x_0 and, differs from those corresponding to all the other states of U for at least an input $u_{[t_0,t)}$.

As in [23] and [22], the local weak observability property can be verified by means of the sufficient rank condition. To this regard, it can be proved the following Theorem.

Theorem 1. The nonlinear system (2.12) and (2.13) is locally weakly observable if the observability matrix $O(x)$, given by:

$$O(x) = \begin{bmatrix} dh(x) \\ dL_f h(x) \\ dL_f^2 h(x) \\ \cdots \end{bmatrix} \tag{2.1}$$

has rank *n.*

As is well known, we have:

$$dh(x) = \frac{\partial h}{\partial x},\ dL_f h(x) = \frac{\partial h}{\partial x} f(x),$$

and:

$$L_f^j h(x) = L_f (L_f^{j-1} h(x))$$

2.1 Model of the 2-branch Model

In this thesis, the 2-branch physical model represented in Fig. 2.1 will be considered for the study of the Supercapacitor.

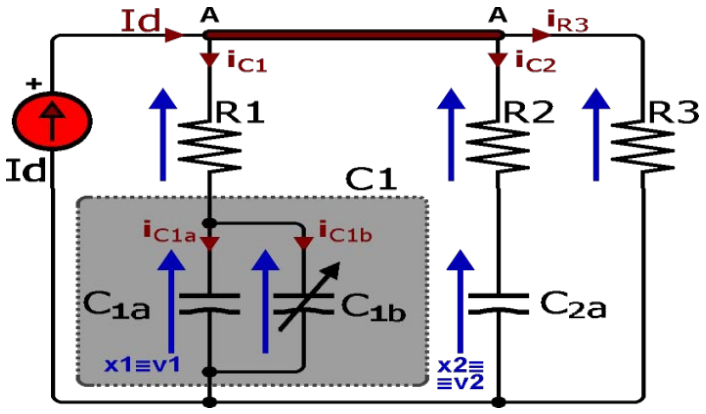

Figure 2.1 – Schematics of a DLC equivalent circuit.

With reference to this model, the following mathematical model is easily obtained, assuming that the circuit of Fig. 1.12 is supplied by an ideal current generator I_d. We have:

$$I_d = i_1 + i_2 + i_3 \tag{2.2}$$

where i_1, i_2 and i_3 are, respectively, the currents flowing on R_1, R_2 and R_0. The currents i_1 and i_2, in terms of the state variables, x_1 and x_2, are given by:

$$i_1 = \frac{y - x_1}{R_1} \qquad i_2 = \frac{y - x_2}{R_2} \tag{2.3}$$

where $y = R_3 i_3$ is the output voltage. From (2.2) and (2.3), the current i_3 is obtained in terms of the state variables, by means of the following equation:

$$\frac{R_3 i_3 - x_1}{R_1} + \frac{R_3 i_3 - x_2}{R_2} + i_3 = I_d$$

which gives:

$$i_3 = \frac{R_2}{\gamma} x_1 + \frac{R_1}{\gamma} x_2 + \frac{R_1 R_2}{\gamma} I_d \tag{2.4}$$

where:

$$\gamma = R_1 R_2 + R_2 R_3 + R_1 R_3$$

Substituting (2.4) into (2.3), we obtain:

$$i_1 = \frac{R_2 + R_3}{\gamma} x_1 + \frac{R_3}{\gamma} x_2 + \frac{R_2 R_3}{\gamma} I_d \tag{2.5}$$

$$i_2 = \frac{R_3}{\gamma} x_1 + \frac{R_1 + R_3}{\gamma} x_2 + \frac{R_1 R_3}{\gamma} I_d \tag{2.6}$$

On the other end, the currents i_1 and i_2 can be expressed in terms of the derivatives of the state variables, as follows:

$$i_1 = C_{1,d} \dot{x}_1 = (C_{1,a} + 2k_1 x_1) \dot{x}_1 \tag{2.7}$$

$$i_2 = C_{2,\mathrm{a}} \dot{x}_2 \tag{2.8}$$

From (2.5) and (2.7), we obtain:

$$\dot{x}_1 = \frac{1}{(C_{1,a} + 2k_1 x_1)}\left(\frac{R_2 + R_3}{\gamma} x_1 + \frac{R_3}{\gamma} x_2 + \frac{R_2 R_3}{\gamma} I_d \right) \tag{2.9}$$

$$\dot{x}_2 = \frac{1}{C_{2,a}}\left(\frac{R_3}{\gamma} x_1 + \frac{R_1 + R_3}{\gamma} x_2 + \frac{R_1 R_3}{\gamma} I_d \right) \tag{2.10}$$

$$y = R_3\left(\frac{R_2}{\gamma} x_1 + \frac{R_1}{\gamma} x_2 + \frac{R_1 R_2}{\gamma} I_d \right) \tag{2.11}$$

Now, defining the state vector $x = \begin{bmatrix} x_1 & x_2 \end{bmatrix}^T$ and putting $u = I_d$, the following state equations are obtained:

$$\dot{x} = f(x) + g(x)u \tag{2.12}$$

$$y = h(x) + du \tag{2.13}$$

where:

$$f(x) = \begin{bmatrix} \frac{1}{(C_{1,a} + 2k_1 x_1)}\left(\frac{R_2 + R_3}{\gamma} x_1 + \frac{R_3}{\gamma} x_2 \right) \\ \frac{1}{C_{2,a}}\left(\frac{R_3}{\gamma} x_1 + \frac{R_1 + R_3}{\gamma} x_2 \right) \end{bmatrix} \qquad b(x) = \begin{bmatrix} \frac{1}{(C_{1,a} + 2k_1 x_1)} \frac{R_2 R_3}{\gamma} \\ \frac{1}{C_{2,a}} \frac{R_1 R_3}{\gamma} \end{bmatrix}$$

$$h(x) = R_3\left(\frac{R_2}{\gamma} x_1 + \frac{R_1}{\gamma} x_2 \right) \qquad d = \frac{R_1 R_2 R_3}{\gamma}$$

It is important to note that in the model (2.12) and (2.13) the state variables are always positive or null.

The model before discussed refers to the description of a cell of SC. Usually, a cell can give voltages of few volts, fo example 2-3 V. In actual applications, in

order to satisfy the requirements on both the current and the voltage that the SC is able to give, several cells of SC are connected in series and in parallel. Also in this case, the physical model of a SC consisting of series and parallel connections of an adequate number of cells is the same as that of a single cell (cf. Fig. 2.1). The mathematical model has the structure (2.12) and (2.13).

2.2 Observability of the SC model

Considering the first two rows of (2.1), we obtain:

$$O_2(x) = \begin{bmatrix} dh \\ dL_f h \end{bmatrix} = \begin{bmatrix} \dfrac{R_2 R_3}{\gamma} & \dfrac{R_1 R_2}{\gamma} \\ \dfrac{\alpha_7 x_1^2 + \alpha_8 x_1 + \alpha_9 x_2 + \alpha_{10}}{(\alpha_5 x_1 + \alpha_6)^2} & \dfrac{\alpha_2 x_1 + \alpha_4}{\alpha_5 x_1 + \alpha_6} \end{bmatrix} \qquad (2.14)$$

where the coefficients γ, p, α_i are constants, and are given by:

$$\gamma = R_1 R_2 + R_1 R_3 + R_2 R_3$$
$$p = R_1 R_2 R_3$$
$$\alpha_1 = 2 R_1 R_3^2 k_1 \gamma$$
$$\alpha_2 = -2(R_1 + R_3) R_1 R_3 k_1 \gamma$$
$$\alpha_3 = \left(R_1 R_{31,a}^2 - 2 R_2^2 R_3 C_{2,a}\right)\gamma$$
$$\alpha_4 = \left(R_2 R_3^2 C_{2,a} - (R_1 + R_3) R_1 R_3 C_{1,a}\right)\gamma$$
$$\alpha_5 = 2 C_{2,a} k_1 \gamma^3$$
$$\alpha_6 = C_{1,a} C_{2,a} \gamma^3$$
$$\alpha_7 = 4 R_1 R_3^2 C_{2,a} k_1^2 \gamma^4$$

$$\alpha_8 = 4R_1R_3^2C_{1,a}C_{2,a}k_1\gamma^4$$
$$\alpha_9 = -2C_{2,a}k_1(R_2R_3^2C_{2,a}\gamma - R_1R_3\left(R_1+R_3\right)C_{1,a}\gamma)\gamma^3 - 2R_1R_3\left(R_1+R_3\right)C_{1,a}C_{2,a}k_1\gamma^4$$
$$\alpha_{10} = C_{1,a}C_{2,a}(R_1R_3^2C_{1,a}\gamma - 2R_2^2R_3C_{2,a}\gamma)\gamma^3$$

According to [16], the model (2.12) and (2.13) is locally weakly observable if the determinant of matrix $O_2(x)$ is different from zero for all *x*. This determinant is given by:

$$\det\left(O\left(x\right)\right) = \frac{\alpha_{11}x_1^2 + \alpha_{12}x_1 + \alpha_{13}x_2 + \alpha_{14}}{\gamma\left(\alpha_5x_1 + \alpha_6\right)^2} \qquad (2.15)$$

and is different from zero for all *x* such that:

$$x_2 \neq ax_1^2 + bx_1 + c \qquad (2.16)$$

where *a*, *b*, and *c* are constants and given by:

$$a = 2\gamma k_1 / R_2C_{2,a}$$
$$b = \left(2C_{1,a} - R_2R_3C_{2,a}\right)/\left(C_{2,a}p\right)$$
$$c = R_1\gamma\left(R_1C_{1,a} - R_2C_{2,a}\right)/\left(2C_{2,a}k_1p\right)$$

The states in which the rank condition is not satisfied belong to a parabola defined as:

$$x_2 = ax_1^2 + bx_1 + c \qquad (2.17)$$

On this curve the observability is not assured since the rank condition is

only a sufficient condition. As a consequence, the observability of the proposed model can be studied by drawing the parabola described by eq. (2.17), on the plane defined by the state variables, and verifying that the trajectory of the operation point does not stay on the parabola itself.

Now, it is useful to study the operation region of an SC on the plane defined by its state variables. In this contest, it should be noted that the coefficient a is always greater than zero, which implies that the parabola concavity is upwards.

The operating region of a SC is defined by its rated voltage. In particular, it is a square on the plane defined by state variables whose boundaries are equal to the rated voltage of the SC.

In general, in the parabola defined by (2.17) we can identify some characteristic points, as the intersection with the axes and the vertex. For obvious reasons, on the observability point of view, it is desirable that the parabola is external to the normal operating region of the SC.

In order to verify in which region of the state plane the above parabola stays, we consider some SC existing in commerce whose parameters are given in the literature. Table 2.1 shows the results of the above research.

Table 2.1 - DLC parameters and values sets for:
the Epcos [1] and Maxwell SC [2]

		R_1, Ω	R_2, Ω	R_3, $k\Omega$	$C_{1,a}$, F	$C_{2,a}$, F	k_1
E. 110 F	(a)	0,010	17,5	5,0	89,0	14,0	29,1
	(b)	0,010	18,3	5,0	84,7	13,0	27,4
E. 200 F	(a)	0,009	8,8	5,0	158,0	27,6	56,2
	(b)	0,009	7,8	5,0	152,7	30,8	58,7
M. 350 F	(a)	0,005	5,5	2,5	232,5	43,2	89,9
	(b)	0,004	7,8	2,5	234,7	30,6	82,2
E. 600 F		0,003	3,1	2,5	454,5	77,4	176,0
M. 83 F		0,010	11	1,1	39,7	11,8	0,9

Table 2.2 shows the expression of the parabola for each SC of Table 2.1. It is apparent in Table 2.1 that, for each SC, the coefficients of the parabola are $a > 0$, $b < 0$ and $c < 0$. It follows that the parabola relative to the SC examined in Table 2.1 has the shape represented in Fig. 2.1, i.e. one intersection on the left half-state plane and the other in the right half plane. The vertex is under the x_1-axis, and, as it can be easily verified, all parabolas are outside the normal region of operation of the corresponding SC, when the SC functions correctly.

Table 2.2 - Parabola equations and its characteristic points, for each DLC.

	Equations / P_1, P_2, P_3, P_V			
	P_1	P_2	$P_3 \cdot 10^3$	$P_V \cdot 10^3$
E.110 (a)	$x_2 = 4.246507x_1^2 - 1728.447x_1 - 2654.953$			
	$(-1.5;0)$	$(408.6;0)$	$(0;-2.6)$	$(0.2;-176)$
E.110 (b)	$x_2 = 4.183435x_1^2 - 1737.109x_1 - 2699.373$			
	$(-1.55;0)$	$(408.6;0)$	$(0;-2.7)$	$(0.2;-180)$
E.200 (a)	$x_2 = 4.082322x_1^2 - 978.9151x_1 - 1384.849$			
	$(-1.4;0)$	$(241.2;0)$	$(0;-1.4)$	$(0.19;-59)$
E.200 (b)	$x_2 = 3.81571x_1^2 - 850.7151x_1 - 1114.561$			
	$(-1.3;0)$	$(224.1;0)$	$(0;-1.1)$	$(0.11;-47)$
M.350 (a)	$x_2 = 4.164707x_1^2 - 1146.061x_1 - 1490.954$			
	$(-1.3;0)$	$(276.5;0)$	$(0;-1.5)$	$(0.14;-79)$
M.350 (b)	$x_2 = 5.369844x_1^2 - 1740.077x_1 - 2497.262$			
	$(-1.43;0)$	$(325.5;0)$	$(0;-2.5)$	$(0.16;-140)$
E.600	$x_2 = 4.562295x_1^2 - 1076.478x_1 - 1394.961$			
	$(-1.3;0)$	$(237.2;0)$	$(0;-1.4)$	$(0.12;-63)$
M.83	$x_2 = 0.1520386x_1^2 - 1090.288x_1 - 24161.45$			
	$(-22.1;0)$	$(7193.2;0)$	$(0;-2.4)$	$(3.58;-1914)$

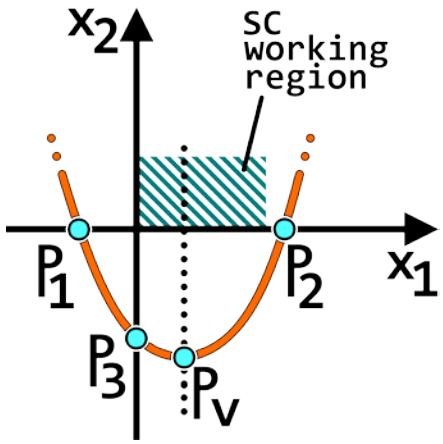

Figure 2.2 – A generic parabola and some characteristic points.

The parabolas are shown in Fig. 2.3. It can be noted that the Epcos DLCs are quite similar to each other, and significantly different from the Maxwell one. In all considered cases, it can be stated that the model of each examined *SC* is observable.

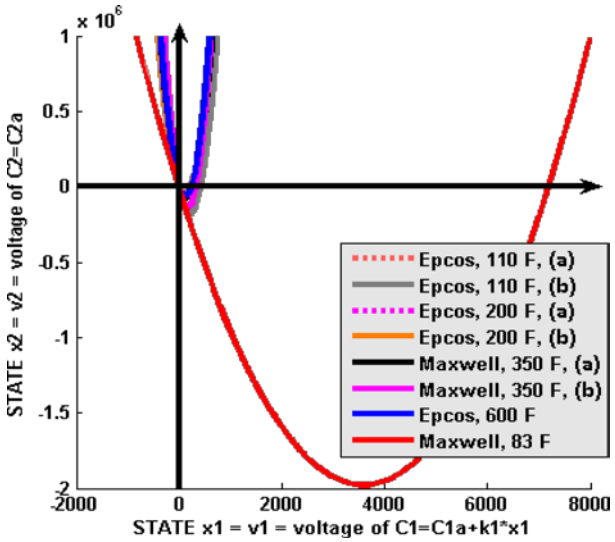

Figure 2.3 – Characteristic parabolas defining the observability region.

A zoom of the parabolas, near to the point P_2 of Fig. 2.3, is shown In Fig. 2.4. It is important to notice that all of the parabolas pass through

the first quadrant for values of x_1 much greater than the actual possible values of x_1 themselves. In all of the considered cases, it can be stated that the model of each examined *SC* is observable.

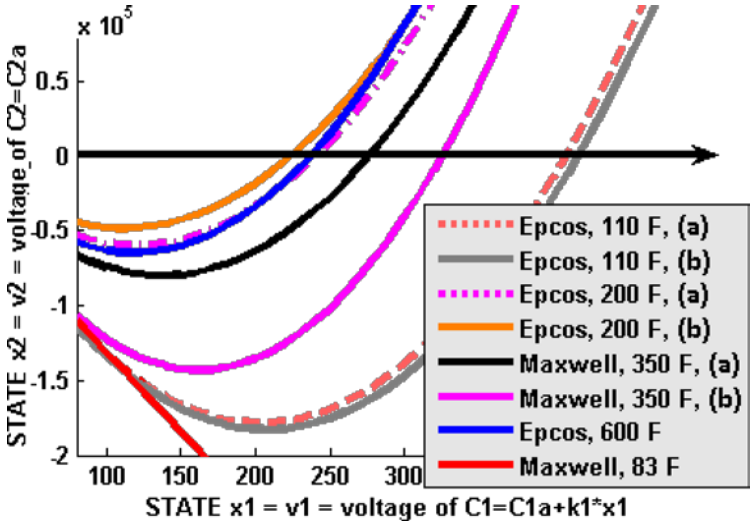

Figure 2.4 – Zoom of the parabolas, near to the point P_2 of the state plane.

Fig. 2.5 shows a zoom of Fig. 2.3 in the neighbourhood of the origin of the state plane. It can be seen that the parabola never crosses the working region in the first quadrant, but touches just 2nd, 3rd and 4th quadrant. In all of the considered cases, it can be stated that the model of each examined *SC* is observable.

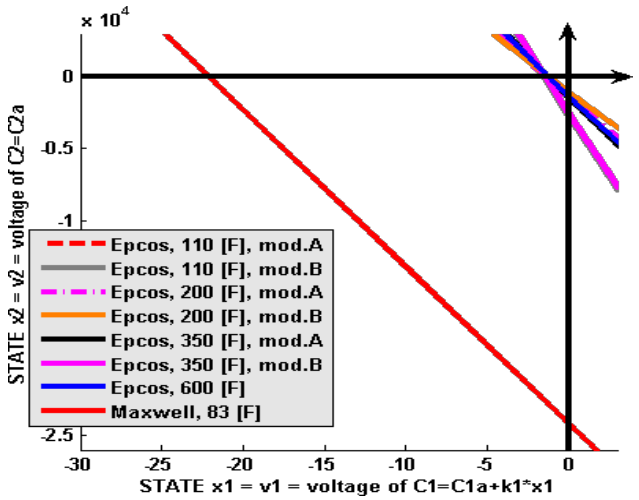

Figure 2.5 – Zoom of the parabolas, near to the origin of the state plane.

2.3 Parametric Analysis

The observability analysis proposed previously has shown that during the normal operating conditions, all of the models of the considered SC are observable.

Indeed, from the two-branch physical model of Fig. 2.1, it is possible to note that the voltage at the SC terminals differs from the voltage at the nonlinear capacitance for the presence of the series resistance R_1. Since this component separates the state variable x_1 from the voltage measured at the SC terminals, it is useful to investigate if increasing R_1 can affect significantly the observability of the system under investigation. To this aim, a fictitious increase of R_1 is introduced. In particular, with reference to the SC Epcos mod. A, it has been increased till it reaches the working region from the relative parabola. This occurs when

$R_1 = 0.55\ \Omega$, and corresponds to the condition $P_2 = (2.3, 0)$, i.e. the intersection of the parabola with the x_1-axis occurs for $x_1 = x_{1N} = 2.3\ \text{V}$. The previous analysis is repeated for all the RC pairs considered in Table 2.1, and the results obtained are given in Fig. 2.5. In this Figure, in the green region observability is guaranteed, but inside the red region nothing can be said about observability, finally the grey region is not of interest. The black diagonal lines is the DLC normal operating region.

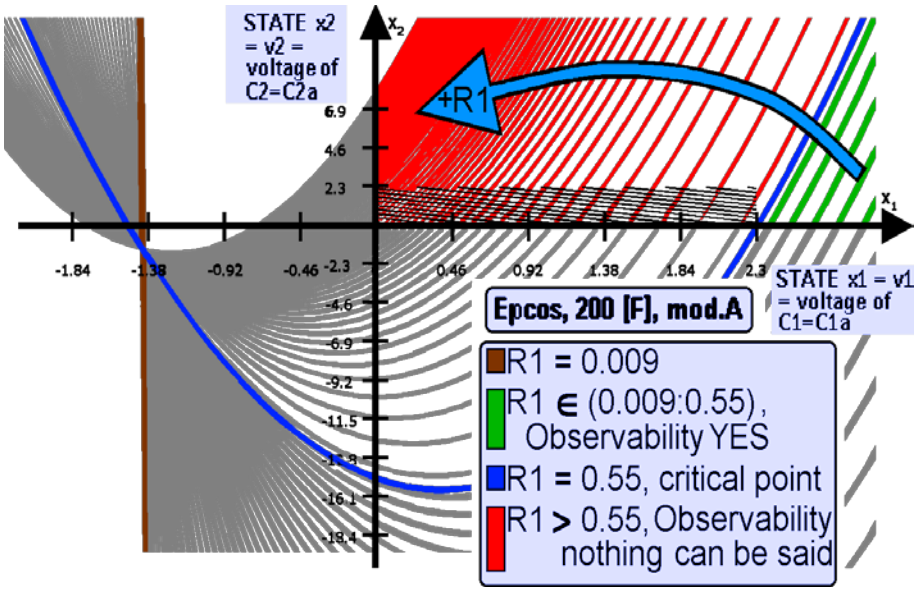

Fig. 2.5 – Dependence of the observability region from R_1.

From the above presented analysis, it can be deduced that, during operating conditions, the SC is observable. If a degradation leads to an increase of R_1, it does not degrade the behaviour of the system until the characteristic parabola reaches the operating region. A further increase of R_1 could imply that the locus of operating point crosses the

characteristic parabola, and in this case the observability is not guaranteed.

Following the parameter estimation (given for example by an observer) particular care has to be taken when the value of R_1 overcomes the critical value, since the observed response might not give an appropriate response.

3 State Estimation by means of Extended Kalman Filter

As already said, the SC health diagnosis is crucial to avoid degradation and failure. In this sense terms such as "life", "lifetime", or "life expectancy" might be used interchangeably. It is essential to first define the SC lifetime. It should be easily quantifiable, for example, as some parameter's threshold when a SC is said to reach its end of life. One common, standard, end-of-life criterion is the decrease of capacitance value to some degree (20% capacitance drop [1-4 7-10] or 30% drop [5 11]) or the 100% increase of the equivalent series resistance [2-7 8-13]. Besides these two common measures, there are some other lifetime parameters as well, such as leakage current or stored energy [2 8]. Among these, the quantity of the energy that can be stored in a SC is closely related to the capacitance value making it, therefore, relatively appropriate as an aging indicator [2, 5, 8, 11].

The life expectancy is often given by manufacturer in the datasheets; as referred to a particular nominal voltage and temperature, as well as a specific cycling pattern. Anyway, during normal operation, these parameters can vary,; as a consequence, it is preferable to have a life estimation system running on-line.

There are two different approaches in literature to characterize a SC lifetime: frequency response based characterization and temporal characterization. The first method aims to identify the SC impedance versus frequency. It is based on the application of a DC voltage and a

low sinusoidal signal superimposed. The SC ageing implies a variation of both the real and imaginary parts of the impedance,; however this method requires a long time to do a sweep and cannot be used with high current [Ageing law for SC, SC ageing by NN].

The temporal characterization is based on the parameters identification using charge or discharge data into a particular assumed model; this approach can be performed in real time. Many papers assume a simple RC series model [State of Health and Life Estimation - Calendar ageing and health diagnosis of supercapacitor]. A more accurate SC model, in which the main capacitance is voltage dependent, would be more appropriate, especially for power electronics applications, since the capacitance can be evaluated at different voltage levels. In particular, for power electronics applications a model with two legs in which the former contains a voltage dependent capacitor with a series resistance and the latter a linear capacitor with a series resistance. As already said, this is the model considered in the present thesis.

The charge stored in a the capacitors is a state variable that can be estimated by a Kalman filter; anyway due to the non-linearity of the SC model an Extended Kalman Filter (EKF) is required.

3.1 Extended Kalman Filter

As is well known, the Kalman Filter is a state estimator for a linear and time-invariant corrupted by white noise, using output measurements

corrupted by white noise too. In view of the implementation of the Kalman Filter on digital devices, we present the KF for discrete-time systems described by the equations:

$$x_{k+1} = A_k x_k + B_k u_k + w_k \tag{3.1}$$

$$y_k = C_k x_k + D_k u_k + v_k \tag{3.2}$$

where x_k, u_k and y_k are, respectively, the state, input and output at the discrete instant *k*, w_k and v_k are the system and measurement noises, respectively, at the instant *k* and A_k, B_k, C_k and D_k are the matrices of the dynamical model assumed time-variant. Usually, it is assumed that the system and measurement noises are uncorrelated between them and with the state and output variables. Moreover, they are Gaussian and white noises with covariance matrices $Q_k = E\left\{w_k w_k^T\right\}$ and $R_k = E\left\{v_k v_k^T\right\}$, where $E\{\cdot\}$ is the expected value of $\{\cdot\}$.

The Kalman Filter algorithm for the system (3.1) and (3.2) is given by [24]:

$$L_k = M_k C_k{}^T \left(R_k + C_k M_k C_k{}^T\right)^{-1}$$

(3.3)

$$\hat{y}_k = C_k \tilde{z}_k + D_k u_k \tag{3.4}$$

$$z_k = \tilde{z}_k + L_k (y_k - \hat{y}_k) \tag{3.5}$$

$$P_k = M_k - L_k C_k M_k \tag{3.6}$$

$$\tilde{z}_{k+1} = (I + A_k) z_k + B_k u_k \tag{3.7}$$

$$M_{k+1} = A_k P_k A_k^T + Q_k \tag{3.8}$$

where:

- $\tilde{z}_k$ is the state predicted at the instant *k* using the state estimated and the input at the instant *k*-1 (cfr. (3.7));
- $\hat{y}_k$ is the output estimated at the instant *k* with the state predicted at the instant *k* (cfr. (3.4));
- z_k is the state estimated at the instant *k* using the predicted state and the output measurement at the same instant *k* (cfr. (3.5));
- P_k is the covariance matrix of the state prediction error $\tilde{e}_k = \tilde{z}_k - x_k$, i.e. $P_k = E\left\{\tilde{e}_k \tilde{e}_k^T\right\}$;
- M_k is the covariance matrix of the state estimation error $e_k = z_k - x_k$, i.e. $M_k = E\left\{e_k e_k^T\right\}$;
- L_k is the gain of the Kalman Filter.

The Extended Kalman Filter is an extension of the Kalman Filter to nonlinear dynamical systems, described by:

$$x_{k+1} = f(x_k, u_k, k) \tag{3.9}$$

$$y_k = g(x_k, u_k, k) \tag{3.10}$$

The Extended Kalman Filter algorithm is given by [24]:

$$L_k = M_k C_k{}^T \left(R_k + C_k M_k C_k{}^T \right)^{-1} \tag{3.11}$$

$$\hat{y}_k = g(\tilde{z}_k, u_k, k) \tag{3.12}$$

$$z_k = \tilde{z}_k + L_k (y_k - \hat{y}_k) \tag{3.13}$$

$$P_k = M_k - L_k C_k M_k \tag{3.14}$$

$$\tilde{z}_{k+1} = z_k + f(z_k, u_k, k) \tag{3.15}$$

$$M_{k+1} = A_k P_k A_k^T + Q_k \tag{3.16}$$

where:

$$A_k = \left. \frac{\partial f(x_k, u_k, k)}{\partial x_k} \right|_{x_k = z_k} \quad , \quad C_k = \left. \frac{\partial f(x_k, u_k, k)}{\partial x_k} \right|_{x_k = z_k}$$

3.2 Designing the Extended Kalman Filter

Assuming that the parameters of the SC are known, the design of EKF is completed by choosing the covariance matrices ***Q*** and ***R***.

To this end, a suitable experiment – consisting of a charge of SC at a constant current $u_k = I_d$ up to the rated value of the output $v_o = V_o$, followed by a free discharge ($u_k = 0$), up to $t = t_d$ and then a discharge at a constant current $u_k = -I_d$ up to $v_o = 0$ has been done. During this experiment, the sequence of data of the output voltage $y_{s,k}$, $k = 1, \cdots, N$, are acquired.

The same sequence u_k, $k = 1, \cdots, N$, generated in the experiment is applied to the model (2.12)-(2.13) obtaining the sequence of output voltage y_k,

$k = 1, \cdots, N$, estimated by the EKF. The sequences $y_{s,k}$ and y_k, allows to define the performance index *J* given by:

$$J = \sum_{i=1}^{N} \left(y_{s,k} - y_k \right)^2 . \tag{3.17}$$

Then, the following optimization problem can be formulated. Given the SC model (2.12)-(2.13) and the corresponding EKF (3.11)-(3.16), determine the covariance matrices Q and R of the noises w_k and v_k, respectively, so that the performance index (3.17) is minimized, subject to the constraints $Q > 0$ and $R > 0$.

The minimization procedure of the performance criterion *J* (cfr. (3.16)) is carried out by using a Genetic optimization algorithm.

The procedure described above algorithm is applied for designing the EKF for the Supercapacitor package Maxwell SC module BMOD0083-P048-B01 having the following main characteristics:

- Rated Capacitance: 83 F
- Minimum Capacitance, initial: 83 F
- Resistance R_1: $R_1 = 0.01\Omega$
- Rated Voltage: 48 V
- Absolute Maximum Voltage: 51 V
- Maximum Continuous Current (ΔT = 15C°): 61 A_{RMS}
- Maximum Continuous Current (ΔT = 40C°): 100 A_{RMS}
- Maximum Peak Current, 1 second (non repetitive): 1100 A

The set of parameters of the SC module, identified as described in [2], are given by:

$$R_1 = 0.01\ \Omega, \quad R_2 = 10\ \Omega, \quad R_3 = 1120\ \Omega,$$
$$C_{1a} = 38\ \text{F}, \quad C_{2a} = 13\ \text{F}, \quad K_{1b} = 0.93\ \text{F/V}$$

The SC module is supplied by means of the sequence of 20000 values of $u_k = I_{d,k}$ represented in Fig. 1.a). This sequence is generated at a frequency of 40 Hz in the interval $[0,500\ \mathrm{s}]$, using the equipment described below, in the Chapter dedicated to the experimental results. The corresponding sequence $y_{s,k}$ is shown in Fig. 1.b).

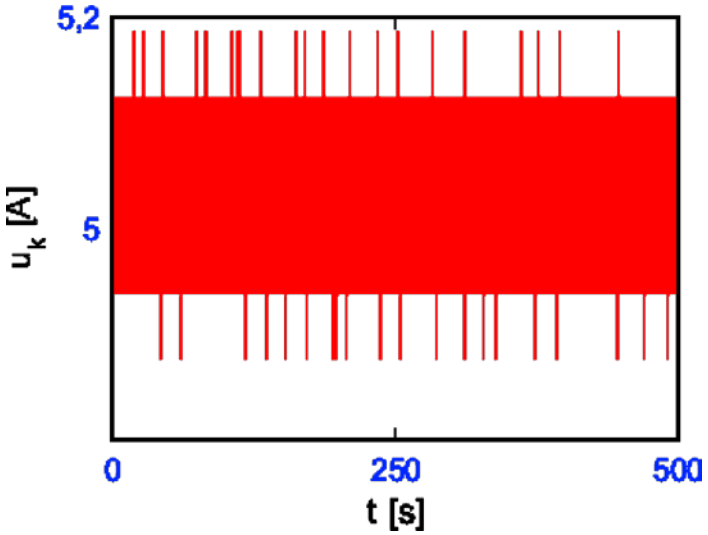

a) Input sequence

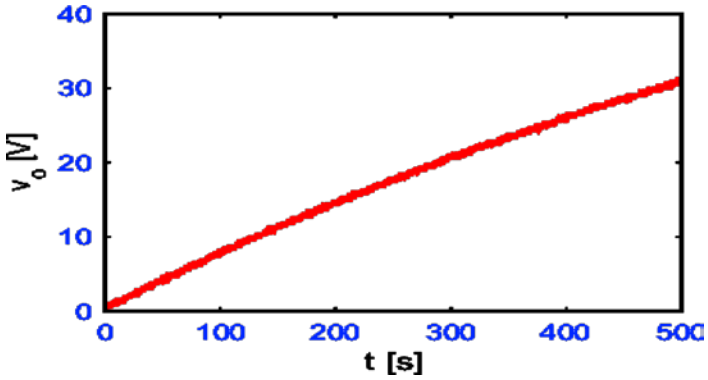

b) Output voltageInput sequence

Fig. 3.1 – Experimental input-output data

The model (2.12) and (2.13) is firstly discretized, using the Euler method, Then, the EKF algorithm (3.11)-(3.16) is implemented in Matlab-Simulink

environment. The Genetic Algorithm at disposal in the Matlab Optimization Tool, is used for minimizing the criterion (3.17). The value $R=1$ is chosen because, as is well known, the responses of the EKF depend on the ratio of the elements of matrix Q and R.

The results obtained are given by:

$$\boldsymbol{Q} = \text{diag}(20,10) \qquad R = 1.$$

As already said, the estimation results do not change if the elements of $\boldsymbol{Q}$ and R are scaled by the same quantity. In particular, inspection of the input current data of Fig. 1 a), shows that the mean and variance of this current are, respectively, 5.0362 and 0.022. It follows that the system and measurement covariance matrices can be scaled by 0.022. In this way, we can choose:

$$Q = \text{diag}(0.0431, 0.02155) \qquad R = 0.022\,.$$

The EKF, supplied by the input current of Fig. 1 a) and the output voltage of Fig. 1 b), with the last parameters $\boldsymbol{Q}$ and R, gives an estimated output which differs from the experimental output voltage as shown in Fig. 2. It can be noticed a convergence towards a zero mean error, confirmed also by means of other experiments.

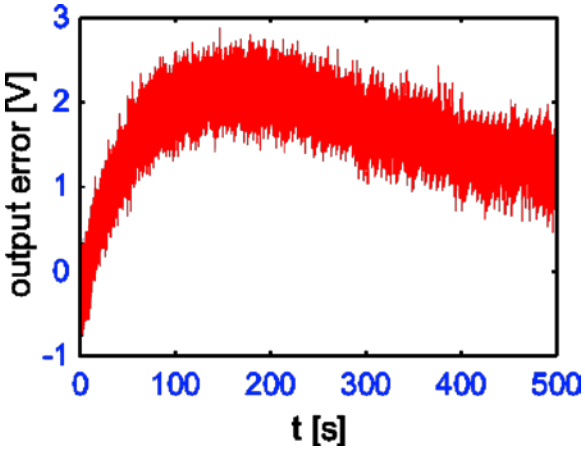

Fig. 3.2. – Output tracking error, with Q=diag(0.0431,0.02155) and R=0.022

3.3 Simulation results

Before to carry out the experimental implementation of the designed EKF, it is convenient to carry out the study of the behaviour of the SC-EKF system by means of simulation experiments. To this end, the SC-model and the EKF algorithm are tested supplying them with the input current given in Fig. 3, corresponding to about three hours of functioning of the system. The corresponding simulation results are given in Fig. 4 and 5.

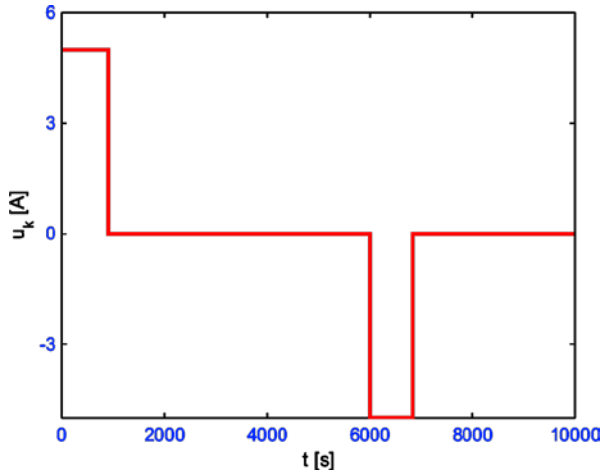

Fig. 3.3 – Waveform of the input current used for simulation.

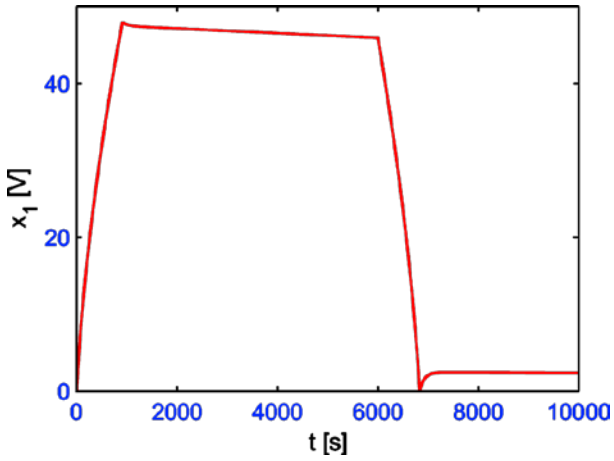

a)

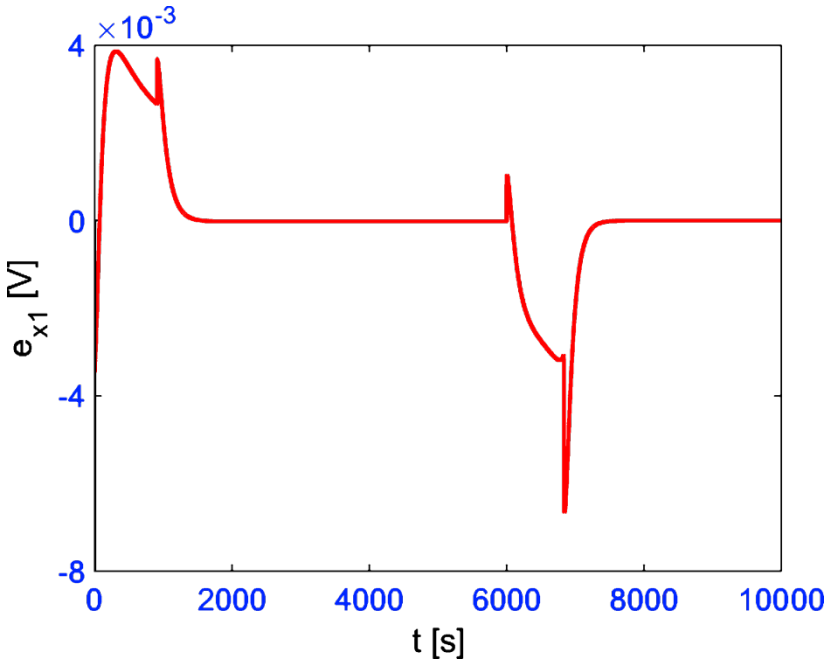

b)

Fig. 3.4 – Response of the SC-EKF system; estimation error $e_{x1} = x_1 - z_1$ **.**

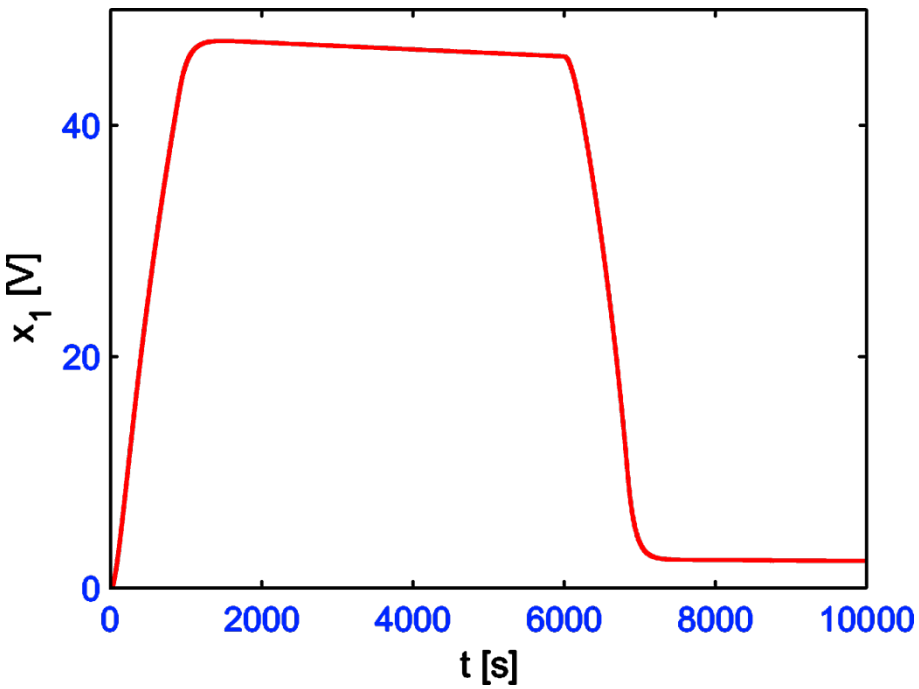

a)

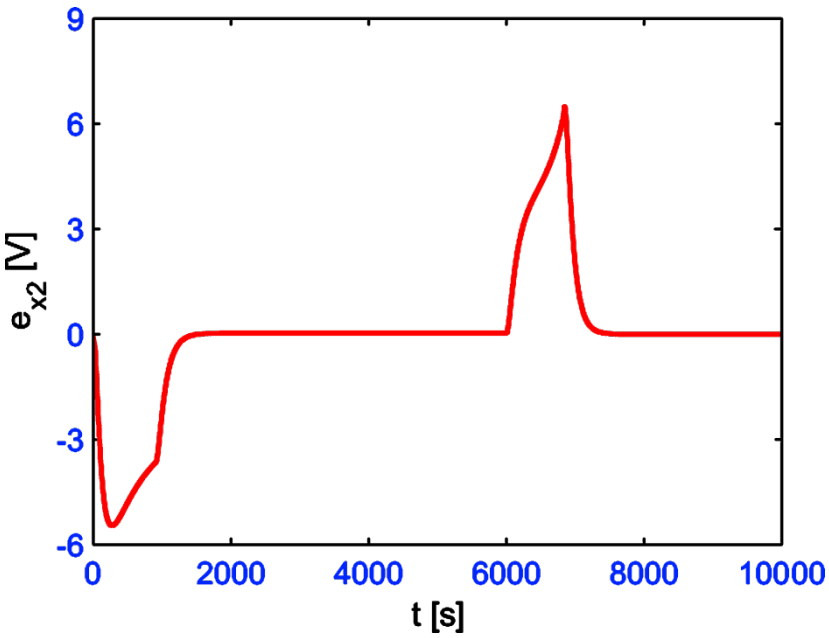

b)

Fig. 3.5 – Response of the SC-EKF system; estimation error $e_{x2} = x_2 - z_2$.

Examination of Fig. 4 shows that the variable x_1 is reproduced perfectly from EKF, which is due to the fact that this variable coincides practically with the output voltage, since the value of the resistance R_1 is very low.

In Fig. 5, it is shown that the estimation error of the variable x_2 is higher than that of x_1 during the phases of charging and discharging at constant current, but it is practically null during the discharging at null input current. However, results obtained allows to conclude that the approach followed in effective for establishing the "health" status of the SC.

4 Experimental verification of the EKF performance

In this section the experimental verification of the parameters estimation by the extended kalman filter on the basis of experimental measurements is shown. In particular, the unknown parameters are the state variables, they are estimated on the basis of electric measurements at the terminals of the supercapacitor under study.

The estimator is realized by the Extended Kalman Filter, or "EKF", since it is an optimal estimator for system models with additive independent white noises. It is the extension of Kalman Filter, or "KF", for nonlinear systems; it firstly linearizes the nonlinear system along a working point, and finally it applies KF equations.

In the case under study, the parameters of interest are the parasitic resistance and the stored charge, they are not directly accessible and measurable to users and gives a information about working life of the supercapacitor.

4.1 The experimental set up

The experimental set up has been arranged at the Institute on Intelligent Systems for the Automation (ISSIA) of the Italian National Research Council (CNR) under the supervision of Eng. Gianpaolo Vitale. The ISSIA was born in 2002 starting from the late reorganization of CNR and is composed of 3 locations, respectively Bari, Genova and Palermo. The section of Palermo, in particular, is involved mainly in the following

thematic subjects: distributed generation from Renewable Sources (RES), variable speed electrical drives, their control, identification, diagnostics and reliability, electromagnetic conducted interference (EMI) and Power Quality, applications of power electronics and electrical drives in electric vehicles, design of power converters and corresponding control systems, electromagnetic compatibility (EMC).

A test bench has been built to acquire electrical data coming from the supercapacitor under test. A *SC-Toolbox* for Matlab+Simulink environment has been developed, which is able to: analyze collected data, apply the EKF, apply a time-windowed EKF, extract all useful data. The laboratory setup is shown in Figure 4.1; it is composed of a power supply, the supercapacitor, the resistor load the switch and the sensors. Measurements are performed by dSPACE system where the software is implemented, a multimeter, the voltage and current sensor board and a laptop. The Main components of the experimental rig are summarized in table 4.1.

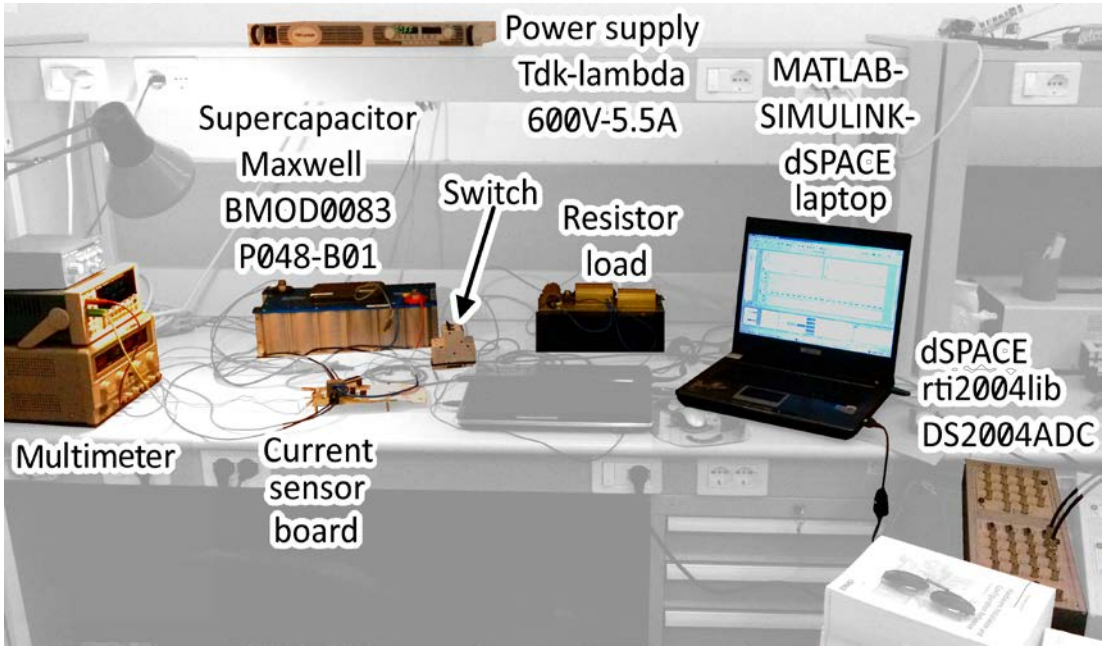

Figure 4.1 – Laboratory Setup.

Table 4.1: Main components of the experimental rig

supplier	function	code
TDK-Lambda	Power Supply	TDKGEN60-40
Maxwell Technologies	Supercapacitor Sensor Board	BMOD0083P048B01
Sorensen	Electronic Load	SLH500V-6A
RS-Components	Resistor passive Load	RS136-238200W3R3J01.03
ABB	Double Pole Switch	S8025UCK32500Vdc50kA
Asus	Laptop PC	
MathWorks	Software	MATLAB7.4, Simulink 6.6.1
dSPACE	Hardware Device	dSPACESYSTEM 3.3.0.7
dSPACE	Hardware DAQ Board	RTI2004LIB DS2004ADC
Tektronix	Digital Multimeter	DMM4050 $6\frac{1}{2}$-Digit

The power supply TDK lambda is used as current generator. It can supply up to 40 A with a maximum voltage of 60 V. It can be remarked that the rated voltage of the supercapacitor is 48 V, hence the power supply has an inherent limitation fixed to 46 V to preserve the supercapacitor.

The supercapacitor is the Maxwell model BMOD0083 P048 B01, it is shown in figure 4.2, the main characteristic parameters of the modules are the following:

- Rated Capacitance: 83 F
- Minimum Capacitance, initial: 83 F
- Maximum ESRDC, initial: 10 mΩ
- Rated Voltage: 48 V
- Absolute Maximum Voltage: 51 V
- Maximum Continuous Current (ΔT = 15C°): 61 ARMS
- Maximum Continuous Current (ΔT = 40C°): 100 ARMS 130
- Maximum Peak Current, 1 second (non-repetitive): 1,100 A

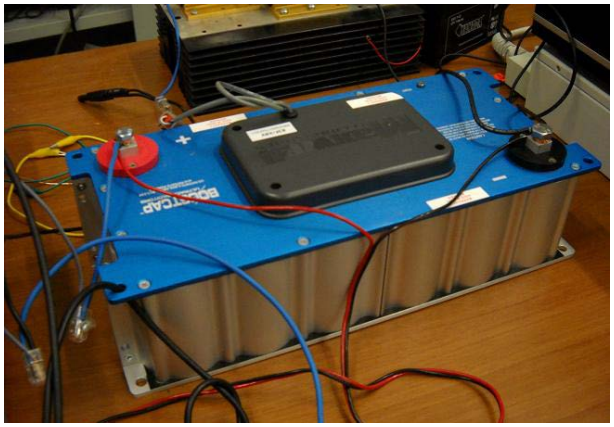

Figure 4.2 – The supercapacitor module

The supercapacitor discharge is performed by the electronic load SLH 500V-6A, it is able to behave as a current sink up to 6 A or by a passive load. In this last case, an exponential discharge is obtained.

The *SC-TOOLBOX* (see Figs. 4.3 part I and II) permits to automate the process of data acquisition, analysis and estimation. This toolbox consists in a long coding script (for inserting *SC* physical data and other relevant values, such as t_0, T_s, or *EKF* parameters), and in a SIMULINK file (processing y) for performing parametric estimation through *EKF* and windowed-*EKF*, *wEKF*, which engages y. The block "*Interceptor*" has the great importance of finding – through relevant instants – the values assumed by EKF behaviour meanwhile it works with the output y.

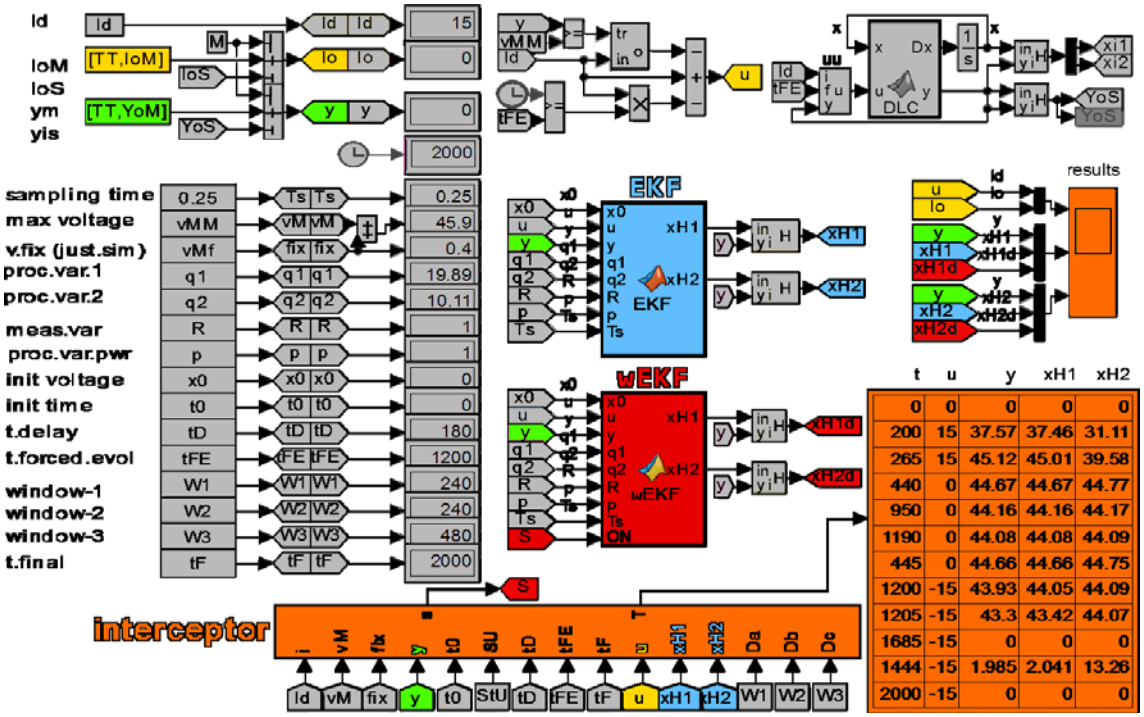

Figure 4.3 – SC-Toolbox, part I.

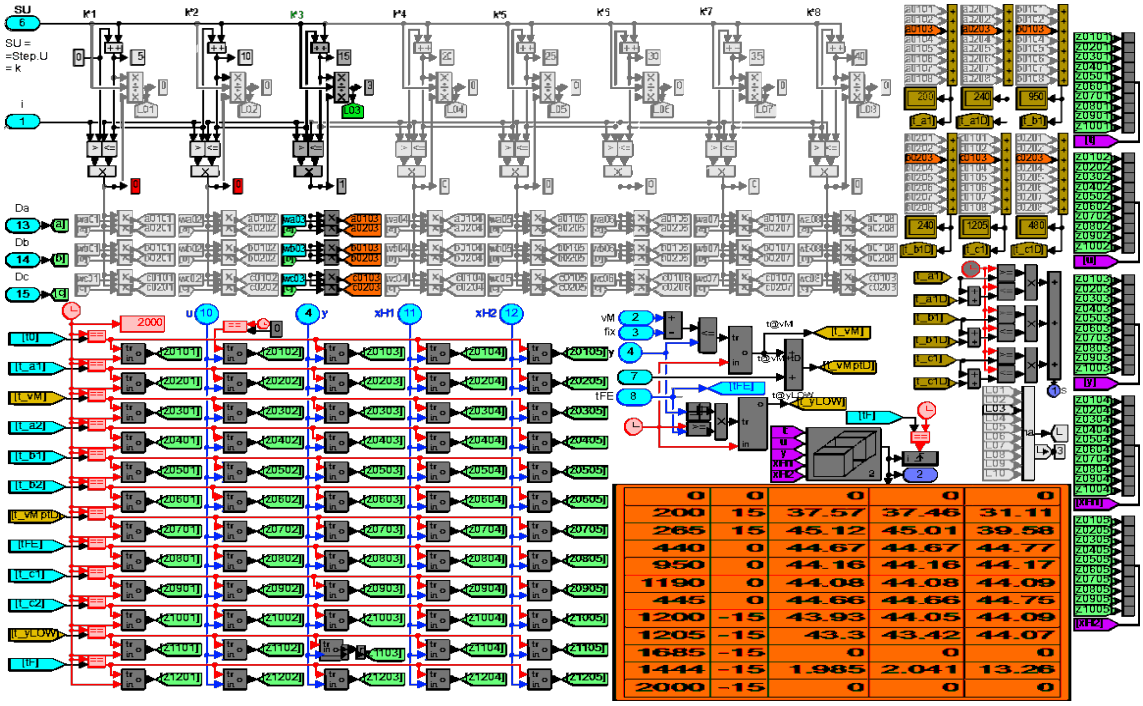

Figure 4.3 – SC-Toolbox, part II.

4.2 Experimental results

The estimation process has been verified performing eight tests characterized by different values of the current supplying the supercapacitor. This current has been set respectively to:

$$I_d = \{ 5, 10, 15, 20, 25, 30, 35, 40 \} \text{ A} \qquad (4.1)$$

After each test numeric, graphical results have been obtained. All results were found by following the table 4.2, in which "G" means "given" by user, "I" means "intercepted" by *EKF*.

Table 4.2 - P SC working times, for measurements and EKF estimation.

Instant(s)	G/I	Description	Phase(s)
t_0	G	Initial time, for charging	Charge
t_{a1}	G	Start of 1st EKF time window	”
t_{VM}	I	Time in which $y = y_{max}$; starting	Free Discharge
t_{a2}	I	End of 1th EKF time window	”
t_{b1} ; t_{b2}	G;I	2nd EKF time window extrema	”
$t_{VM} + t_D$	I+G	Fixed time range (180 *s*)	”
t_{FE}	G	Initial time, for forced evolution	Forced Discharge
t_{c1} ; t_{c2}	G;I	3rd EKF time window extrema	”
$t_{y=2}$	I	Time after which *y* is fairly low	”
t_F	G	Initial time, for free evolution Final time	”

With reference to the times t_{V_M} and $t_{V_M} + t_D$. t_{V_M} , although the SC datasheet declares a maximum value achievable, in real measurements a lower value is used, not to force the SC itself. $t_{V_M} + t_D$: this time range starts when y reaches its maximum value and it is fixed to 180 s for each measurement; it points out the voltage loss during the free discharge. It is important to notice that the initial condition for free evolution is the same for each measurements; hence, assumed value at $t_{V_M} + t_D$ is almost the same for each measurement. The Table 4.3 shows the window time ranges (1^{st} window is $t_{a1} \sim t_{a2}$, 2^{nd} window is $t_{b1} \sim t_{b2}$, 3^{rd} window is $t_{c1} \sim t_{c2}$; times expressed in seconds), for different values of $I_d = \{5, 10, 15, 20, 25, 30, 35, 40\}$A.

Table 4.3: wEKF windows working times.

t \ Id	5	10	15	20	25	30	35	40
t_{a1}	700	300	200	140	120	90	75	70
t_{a2}	940	940	540	440	380	360	315	310
t_{b1}	950	950	950	950	950	950	950	950
t_{b2}	1190	1190	1190	1190	1190	1190	1190	1190
t_{c1}	1250	1250	1250	1250	1250	1250	1250	1250
t_{c2}	1750	1750	1720	1720	1710	1710	1710	1710

Finally, for each measurements, a table and two multiple output plots have been drawn. The table shows time values in the first two columns, and the respective values of EKF estimation, when intercepted.

For each test, the first plot is divided in two parts; the upper subplot shows the output current I_o (dotted grey, not in scale; showing it is useful to point out the 3 phases of: charge $t_0 \sim t_{V_M}$, free discharge $t_{V_M} \sim t_{FE}$, forced discharge $t_{FE} \sim t_f$), the output voltage y (in green), the state $\hat{x}_1$ estimated by the *EKF* (in blue), the state $\hat{x}_{1,w}$ estimated by the *wEKF* (in red). The second subplot shows the measure error

between the output y and the estimated value $\hat{x}_1$, $e_1 = y - \hat{x}_1$, showing the maximum and minimum values.

Similarly, the second plot is divided in two parts; the upper subplot shows the output current I_o (dotted grey, not in scale), the output voltage y (in green), the state $\hat{x}_2$ estimated by the *EKF* (in blue), the state $\hat{x}_{2,w}$ estimated by the *wEKF* (in red). The second subplot shows the measure error between the output y and the estimated value $\hat{x}_2$, $e_2 = y - \hat{x}_2$, showing the maximum and minimum values.

Both plots demonstrate, as expected from the model, that the first branch is really faster than the second one. In fact, $\hat{x}_1$ almost perfectly covers the output voltage y. Differently, $\hat{x}_2$ is well distinguishable from y, because of R_2 is almost 10 times greater than R_1. The errors e_1 and e_2, as shown in their respective subplots, are really different. For a diagnostic purpose, the value of $\hat{x}_1$ is more representative – with respect to $\hat{x}_2$ – of the internal SC state, above all during transient time ranges.

Table 4.4: Numeric results, for $I_d = \pm 5A$

time		I_d	y	$\hat{x}_1$	$\hat{x}_2$
$\mathbf{t_0}$	**0**	**5**	**0.0000**	**0.0000**	**0.0000**
t_{a1}	700	5	41.7174	41.6812	39.5181
$\mathbf{t_{yM}}$	**813**	**0**	**45.9274**	**45.5288**	**44.5747**
t_{a2}	940	0	44.5744	44.5745	44.7997
t_{b1}	950	0	44.5140	44.5141	44.7454
t_{b2}	1190	0	43.2517	43.2516	43.4523
$t_{V_M} + t_D$	993	0	44.2689	44.2687	44.5008
$\mathbf{t_{FE}}$	**1200**	**−5**	**43.1845**	**43.2226**	**43.4046**
t_{c1}	1250	−5	25.6696	25.7006	35.4918
t_{c2}	1750	−5	0.1040	0.0000	0.0000
$t_{y=2}$	1457	−5	2.0000	2.0120	5.1164
$\mathbf{t_F}$	**2000**	**−5**	**0.0570**	**0.0000**	**0.0000**

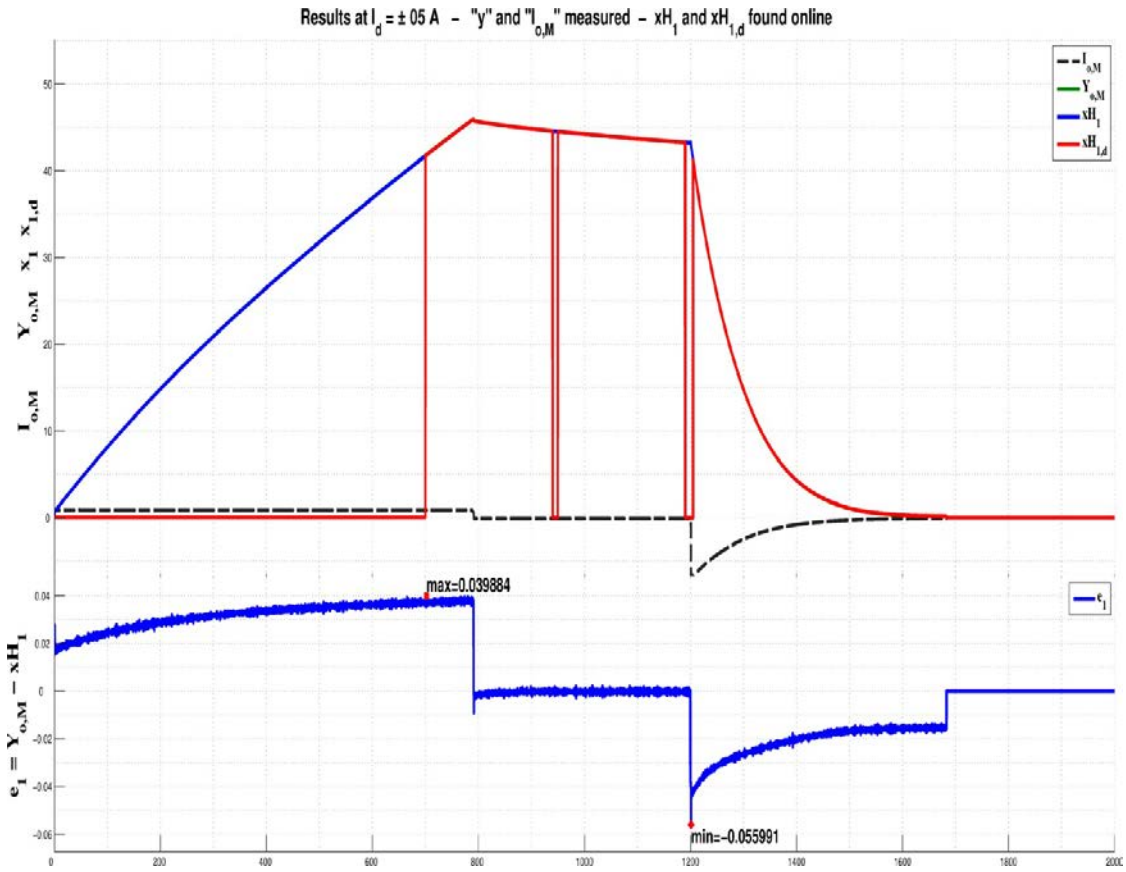

Fig 4.4a – Estimation of $\hat{x}_1$ and $\hat{x}_{1,w}$, with $I_d = \pm 5A$

On top of the fig 4.4a there are the measured current I_o (dotted grey, not in scale; it is useful to point out the 3 phases of: charge $t_0 \sim t_{V_M}$, free discharge $t_{V_M} \sim t_{FE}$, forced discharge $t_{FE} \sim t_f$), the measured voltage y (in green) on SCterminals, the estimated $\hat{x}_1$ by EKF (in blue), the estimated $\hat{x}_{1,w}$ by $wEKF$ (in red). On bottom there is the measure error $e_1 = y - \hat{x}_1$, showing the maximum and minimum values.

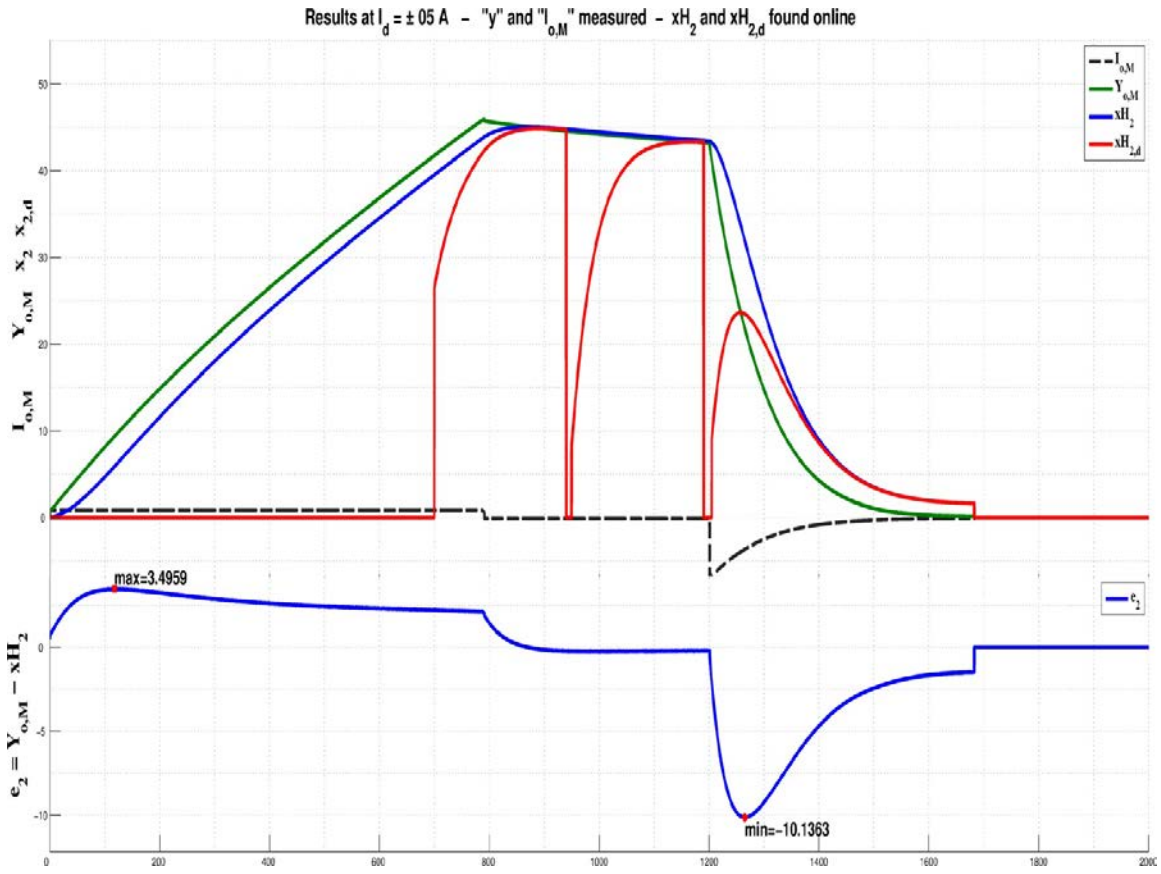

Fig. 4.4b – Estimation of $\hat{x}_2$ and $\hat{x}_{2,w}$, with $I_d = \pm 5A$

On top of the figure 4.4b there are the measured current I_o (dotted grey, not in scale; it is useful to point out the 3 phases of: charge $t_0 \sim t_{V_M}$, free discharge $t_{V_M} \sim t_{FE}$, forced discharge $t_{FE} \sim t_f$), the measured voltage y (in green) on SCterminals, the estimated $\hat{x}_2$ by EKF (in blue), the estimated $\hat{x}_{2,w}$ by $wEKF$ (in red). On bottom there is the measure error $e_2 = y - \hat{x}_2$, showing the maximum and minimum values.

Table 4.5 - Numeric results, for $I_d = \pm 10A$

time		I_d	y	$\hat{x}_1$	$\hat{x}_2$
t_0	**0**	**10**	**0.0000**	**0.0000**	**0.0000**
t_{a1}	300	10	38.1352	38.0614	33.0710
$t_{ум}$	**383**	**0**	**45.7662**	**45.3759**	**41.8590**
t_{a2}	540	0	44.6046	44.6049	44.6677
t_{b1}	950	0	43.7687	43.7680	43.8185
t_{b2}	1190	0	43.4397	43.4402	43.5010
$t_{V_M} + t_D$	563	0	44.5173	44.5185	44.6237
t_{FE}	**1200**	**-10**	**43.4430**	**43.5181**	**43.4939**
t_{c1}	1250	-10	25.8543	25.9194	35.7894
t_{c2}	1750	-10	0.2115	0.2419	3.0150
$t_{y=2}$	1473	-10	2.0000	2.0050	5.7868
t_F	**2000**	**-10**	**0.0973**	**0.0000**	**0.0000**

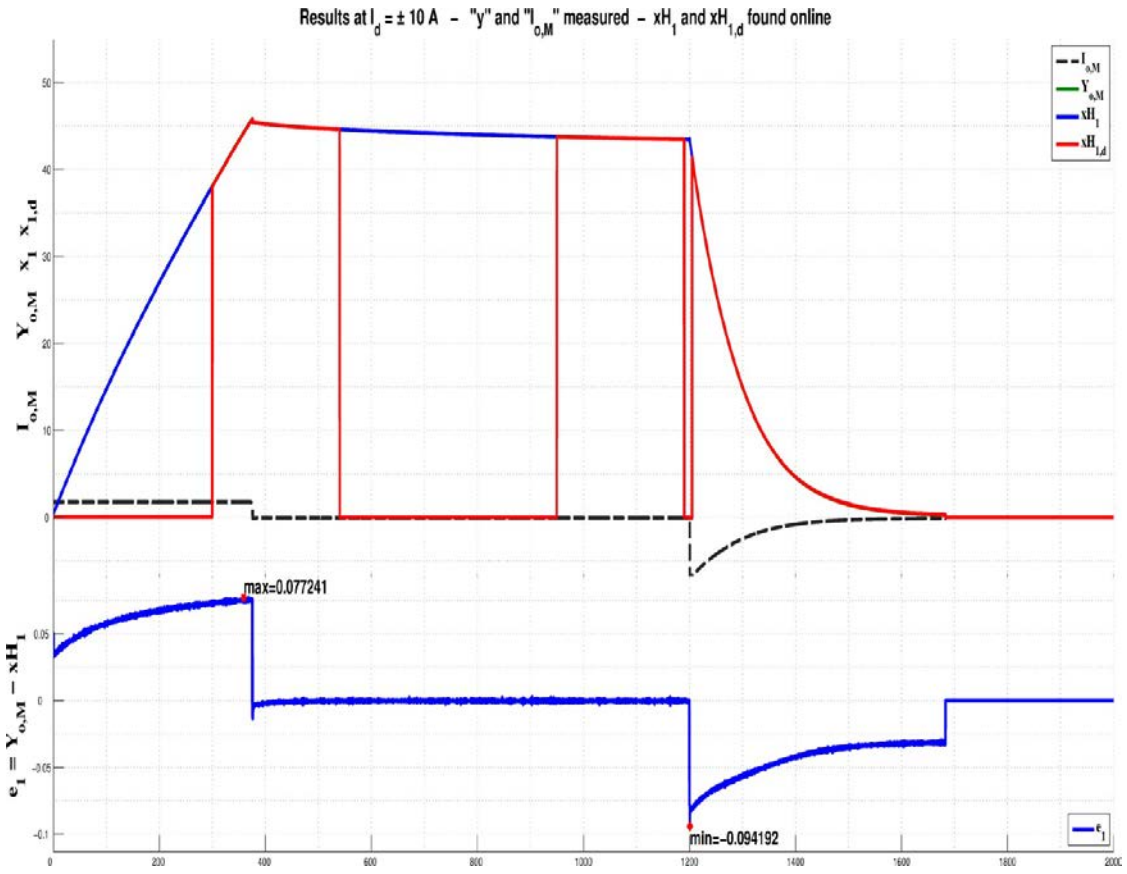

Fig 4.5a – Estimation of $\hat{x}_1$ and $\hat{x}_{1,w}$, with $I_d = \pm 10A$

On top of the fig 4.5a there are the measured current I_o (dotted grey, not in scale; it is useful to point out the 3 phases of: charge $t_0 \sim t_{V_M}$, free discharge $t_{V_M} \sim t_{FE}$, forced discharge $t_{FE} \sim t_f$), the measured voltage y (in green) on SCterminals, the estimated $\hat{x}_1$ by EKF (in blue), the estimated $\hat{x}_{1,w}$ by $wEKF$ (in red). On bottom there is the measure error $e_1 = y - \hat{x}_1$, showing the maximum and minimum values.

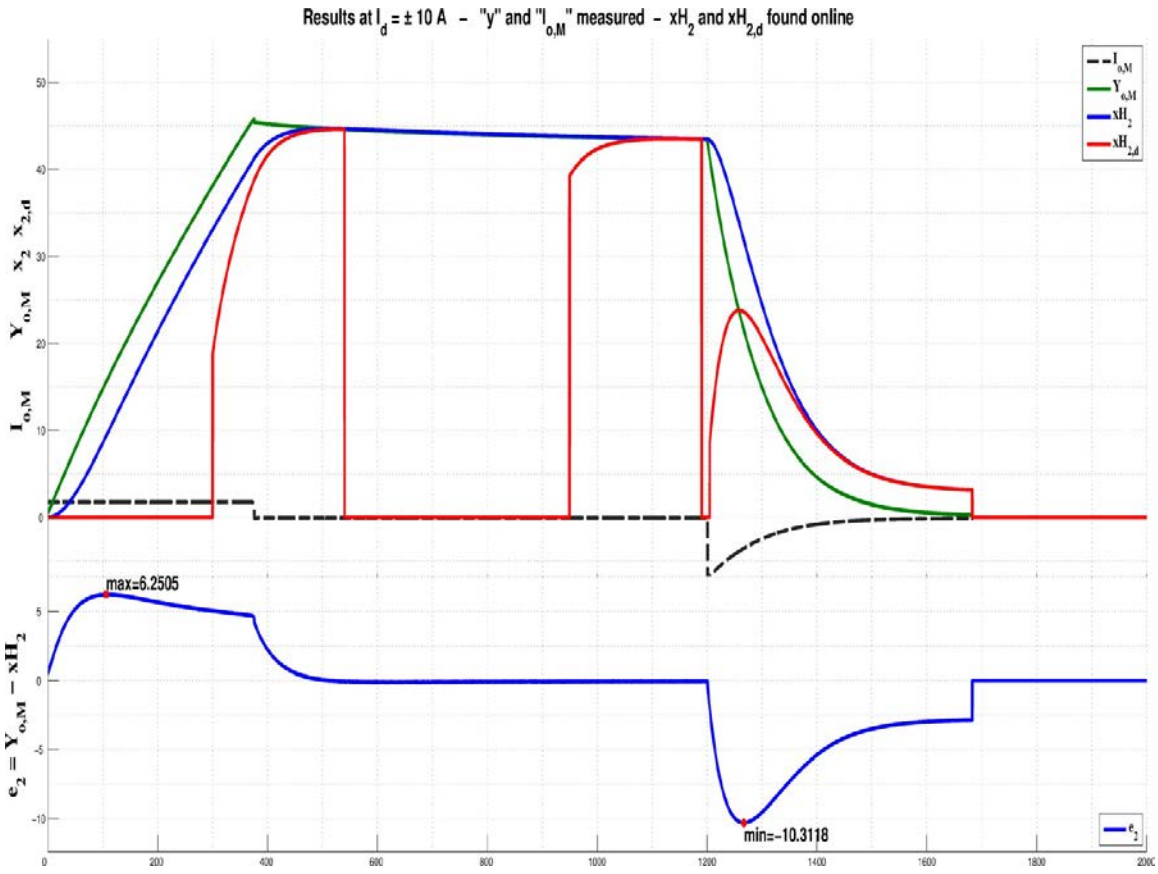

Fig 4.5b – Estimation of $\hat{x}_2$ and $\hat{x}_{2,w}$, with $I_d = \pm 10A$

On top of the figure 4.5b there are the measured current I_o (dotted grey, not in scale; it is useful to point out the 3 phases of: charge $t_0 \sim t_{V_M}$, free discharge $t_{V_M} \sim t_{FE}$, forced discharge $t_{FE} \sim t_f$), the measured voltage y (in green) on SCterminals, the estimated $\hat{x}_2$ by EKF (in blue), the estimated $\hat{x}_{2,w}$ by $wEKF$ (in red). On bottom there is the measure error $e_2 = y - \hat{x}_2$, showing the maximum and minimum values.

Table 4.6 - Numeric results, for $I_d = \pm 15A$

time		I_d	y	$\hat{x}_1$	$\hat{x}_2$
t_0	**0**	**15**	**0.0000**	**0.0000**	**0.0000**
t_{a1}	200	15	38.9308	38.8202	31.0649
t_{yM}	**239**	**15**	**45.5010**	**45.0180**	**37.6786**
t_{a2}	440	0	43.6109	43.6085	43.7506
t_{b1}	950	0	41.5193	41.5190	41.6608
t_{b2}	1190	0	40.6229	40.6223	40.7675
$t_{V_M} + t_D$	419	0	43.7015	43.7017	43.8199
t_{FE}	**1200**	**−15**	**40.5826**	**40.6923**	**40.7355**
t_{c1}	1220	−15	32.8441	32.9552	39.1228
t_{c2}	1720	−15	0.0973	0.0000	0.0000
$t_{y=2}$	1447	−15	2.0000	2.0328	7.1836
t_F	**2000**	**−15**	**0.0637**	**0.0000**	**0.0000**

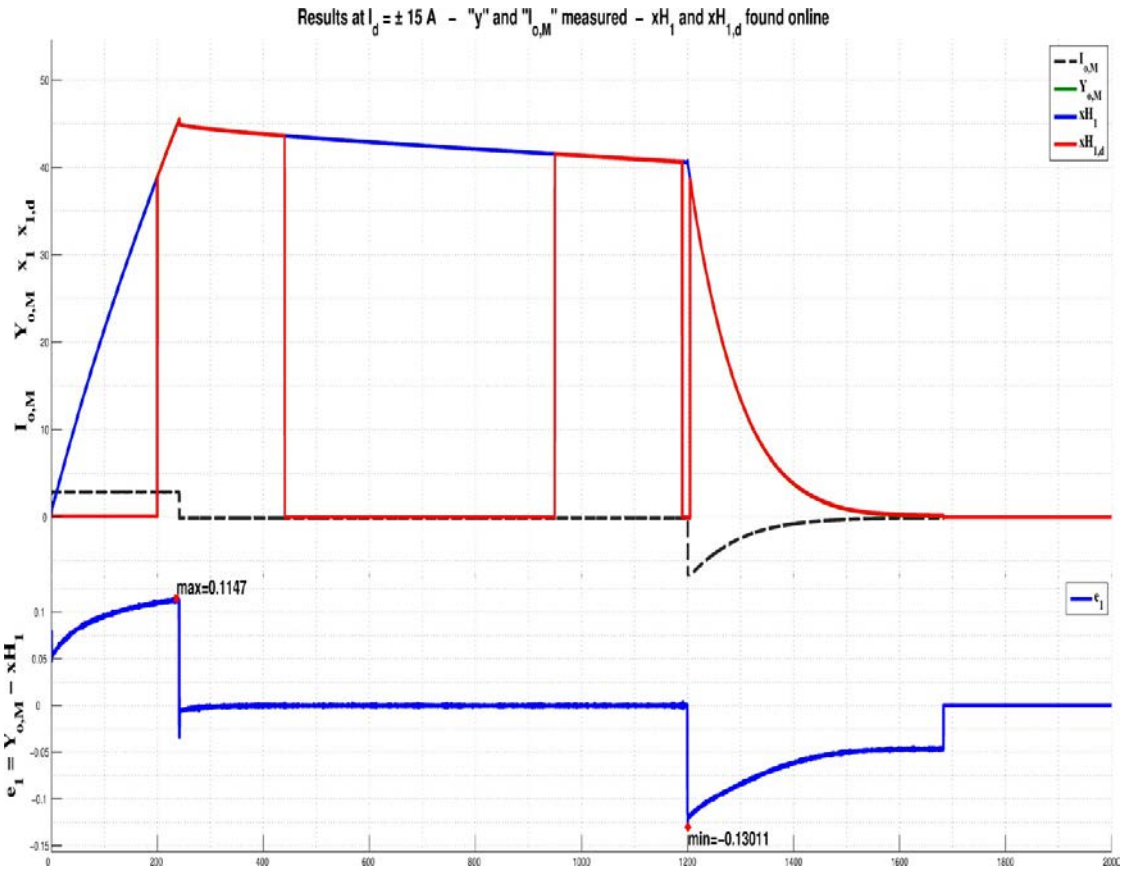

Fig. 4.6a – Estimation of $\hat{x}_1$ and $\hat{x}_{1,w}$, with I_d = ±15*A*

On top of the figure 4.6a there are the measured current I_o (dotted grey, not in scale; it is useful to point out the 3 phases of: charge $t_0 \sim t_{V_M}$, free discharge $t_{V_M} \sim t_{FE}$, forced discharge $t_{FE} \sim t_f$), the measured voltage y (in green) on *SC*terminals, the estimated $\hat{x}_1$ by *EKF* (in blue), the estimated $\hat{x}_{1,w}$ by *wEKF* (in red). On bottom there is the measure error $e_1 = y - \hat{x}_1$, showing the maximum and minimum values.

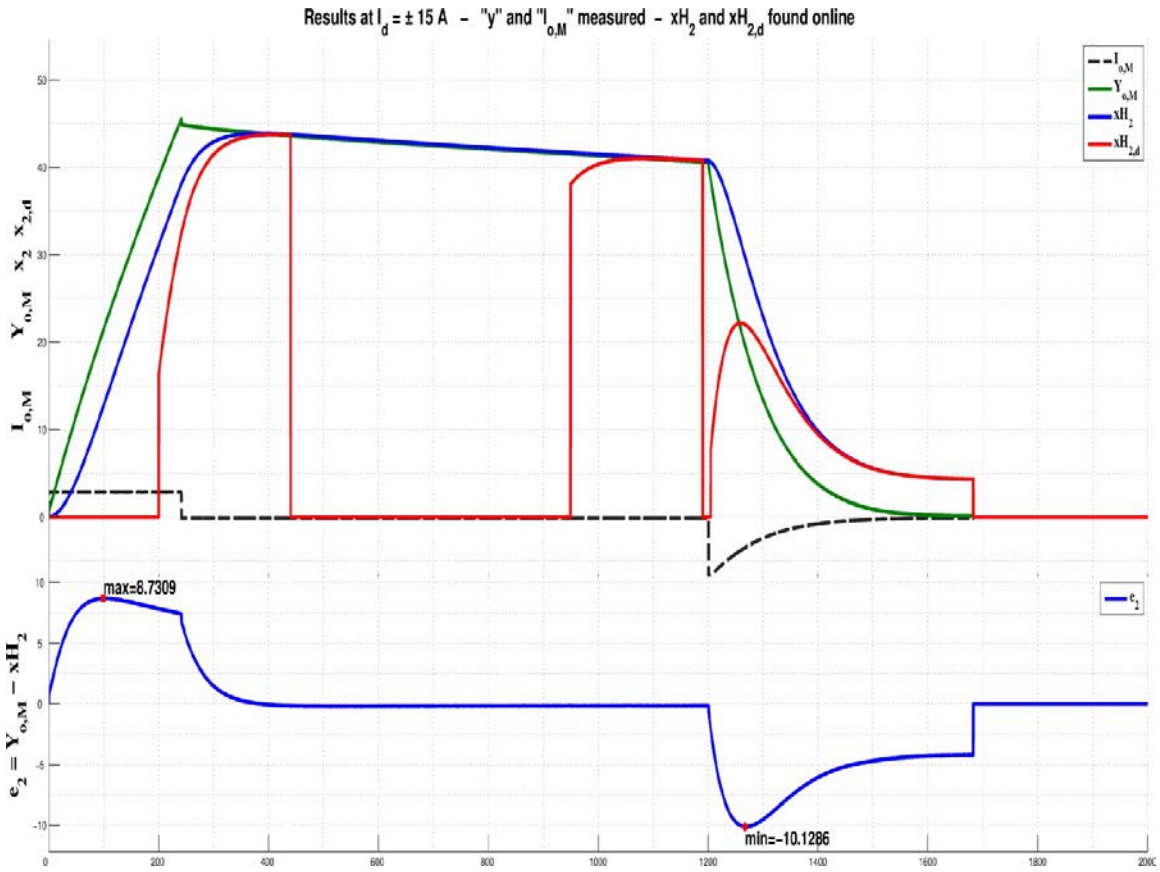

Fig 4.6b – Estimation of $\hat{x}_2$ and $\hat{x}_{2,w}$, with $I_d = \pm 15A$

On top of the figure 4.6b there are the measured current I_o (dotted grey, not in scale; it is useful to point out the 3 phases of: charge $t_0 \sim t_{V_M}$, free discharge $t_{V_M} \sim t_{FE}$, forced discharge $t_{FE} \sim t_f$), the measured voltage y (in green) on SCterminals, the estimated $\hat{x}_2$ by EKF (in blue), the estimated $\hat{x}_{2,w}$ by $wEKF$ (in red). On bottom there is the measure error $e_2 = y - \hat{x}_2$, showing the maximum and minimum values.

Table 4.7 - Numeric results, for $I_d = \pm 20A$

time		I_d	y	$\hat{x}_1$	$\hat{x}_2$
t_0	**0**	**20**	**0.0000**	**0.0000**	**0.0000**
t_{a1}	140	20	36.9635	36.8181	26.3621
t_{y_M}	**177**	**20**	**45.3936**	**44.8505**	**34.9506**
t_{a2}	380	0	43.2651	43.2651	43.3997
t_{b1}	950	0	40.9083	40.9075	41.0578
t_{b2}	1190	0	40.0253	40.0253	40.1662
$t_{V_M} + t_D$	357	0	43.3725	43.3727	43.4633
t_{FE}	**1200**	**-20**	**39.9649**	**40.1118**	**40.1351**
t_{c1}	1220	-20	32.3775	32.5238	38.6244
t_{c2}	1720	-20	0.0940	0.0000	0.0000
$t_{y=2}$	1445	-20	2.0000	2.0579	8.1829
t_F	**2000**	**-20**	**0.0604**	**0.0000**	**0.0000**

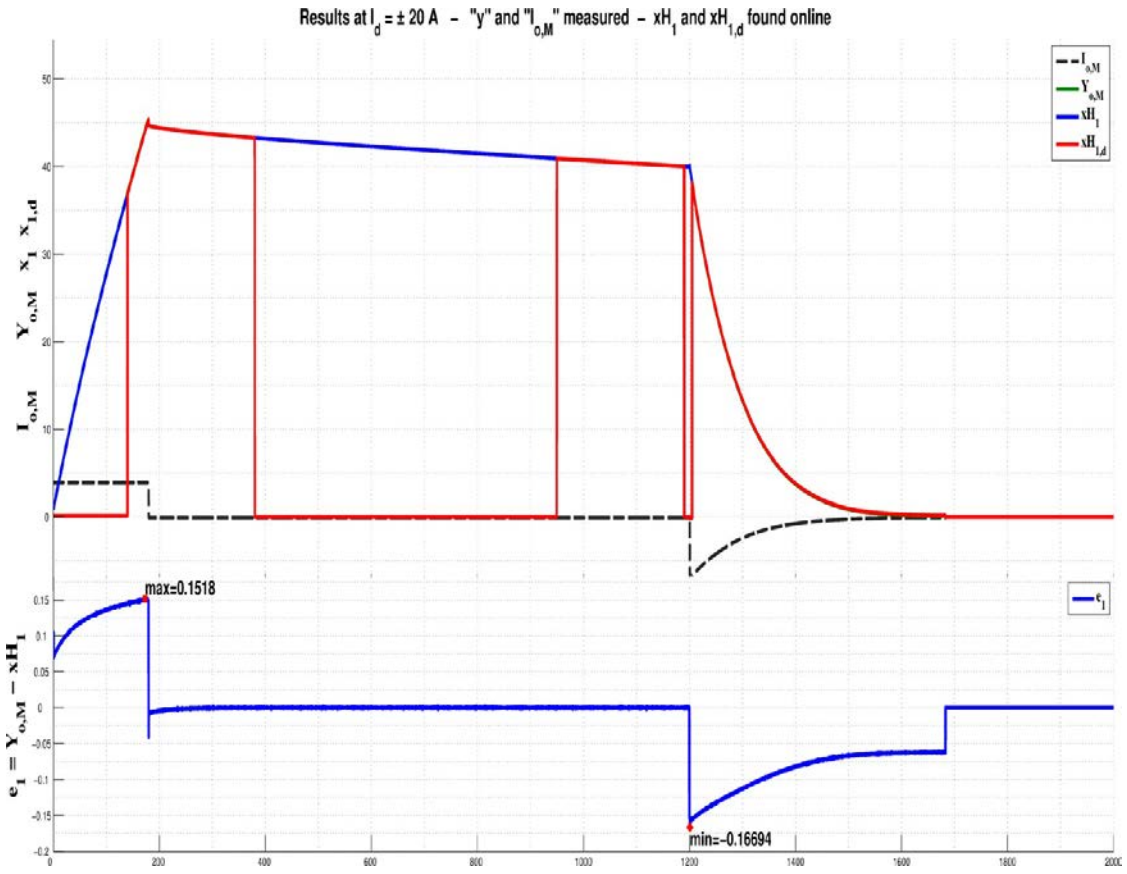

Fig 4.7a – Estimation of $\hat{x}_1$ and $\hat{x}_{1,w}$, with I_d = ±20*A*

On top of the figure 4.7a there are the measured current I_o (dotted grey, not in scale; it is useful to point out the 3 phases of: charge $t_0 \sim t_{V_M}$, free discharge $t_{V_M} \sim t_{FE}$, forced discharge $t_{FE} \sim t_f$), the measured voltage y (in green) on *SC*terminals, the estimated $\hat{x}_1$ by *EKF* (in blue), the estimated $\hat{x}_{1,w}$ by *wEKF* (in red). On bottom there is the measure error $e_1 = y - \hat{x}_1$, showing the maximum and minimum values.

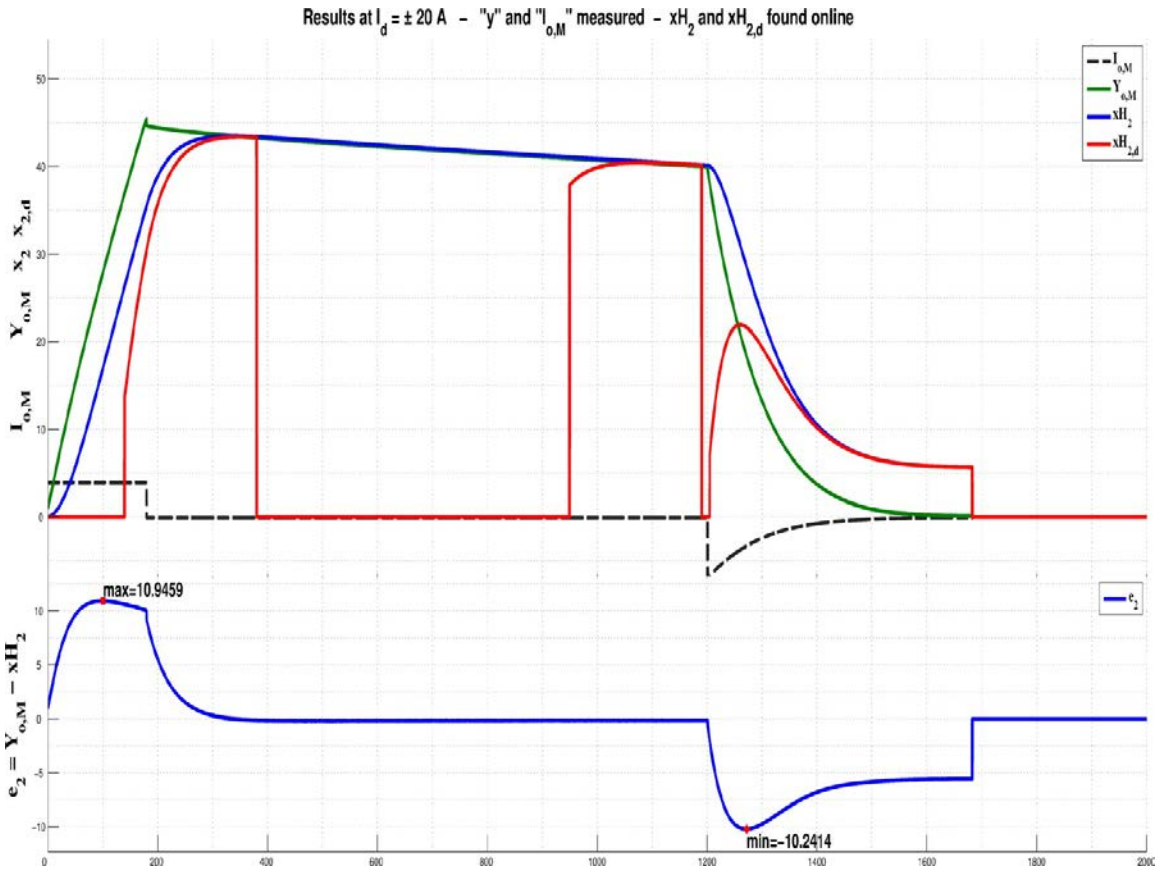

Fig. 4.7b – Estimation of $\hat{x}_2$ and $\hat{x}_{2,w}$, with $I_d = \pm 20A$

On top of the figure 4.7b there are the measured current I_o (dotted grey, not in scale; it is useful to point out the 3 phases of: charge $t_0 \sim t_{V_M}$, free discharge $t_{V_M} \sim t_{FE}$, forced discharge $t_{FE} \sim t_f$), the measured voltage y (in green) on SCterminals, the estimated $\hat{x}_2$ by EKF (in blue), the estimated $\hat{x}_{2,w}$ by $wEKF$ (in red). On bottom there is the measure error $e_2 = y - \hat{x}_2$, showing the maximum and minimum values.

Table 4.8 - Numeric results, for $I_d = \pm 25A$

time		I_d	y	$\hat{x}_1$	$\hat{x}_2$
t_0	**0**	**25**	**0.0000**	**0.0000**	**0.0000**
t_{a1}	120	25	38.4239	38.2411	26.0083
$t_{ум}$	**146**	**25**	**45.2593**	**44.6981**	**32.9268**
t_{a2}	360	0	41.9658	41.9662	42.2034
t_{b1}	950	0	39.0349	39.0340	39.2020
t_{b2}	1190	0	38.0546	38.0541	38.2102
$t_{V_M} + t_D$	326	0	42.1941	42.1939	42.3812
t_{FE}	**1200**	**-25**	**38.0076**	**38.1887**	**38.1770**
t_{c1}	1210	-25	34.0359	34.2238	37.7929
t_{c2}	1710	-25	0.1208	0.1995	6.9952
$t_{y=2}$	1443	-25	2.0000	2.0801	9.1177
t_F	**2000**	**-25**	**0.0436**	**0.0000**	**0.0000**

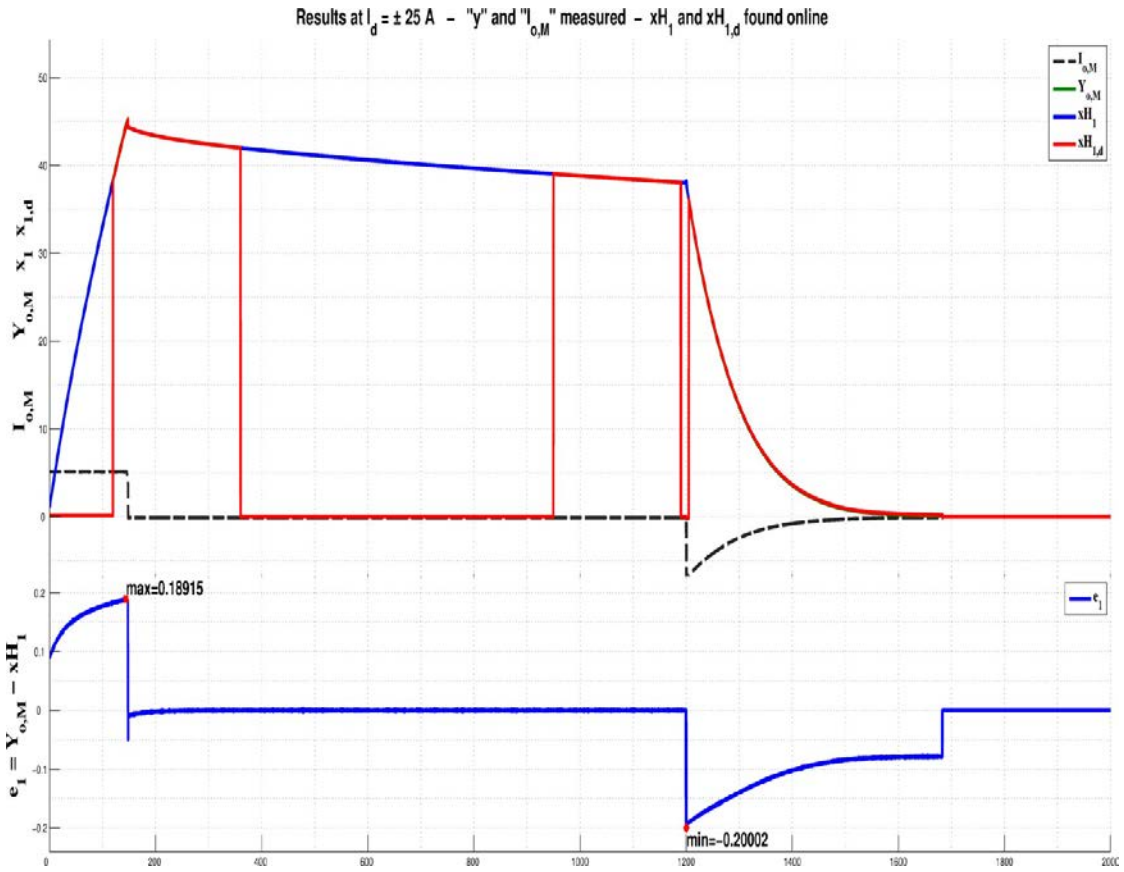

Fig 4.8a – Estimation of $\hat{x}_1$ and $\hat{x}_{1,w}$, with $I_d = \pm 25A$

On top of the figure 4.8a there are the measured current I_o (dotted grey, not in scale; it is useful to point out the 3 phases of: charge $t_0 \sim t_{V_M}$, free discharge $t_{V_M} \sim t_{FE}$, forced discharge $t_{FE} \sim t_f$), the measured voltage y (in green) on SCterminals, the estimated $\hat{x}_1$ by EKF (in blue), the estimated $\hat{x}_{1,w}$ by $wEKF$ (in red). On bottom there is the measure error $e_1 = y - \hat{x}_1$, showing the maximum and minimum values.

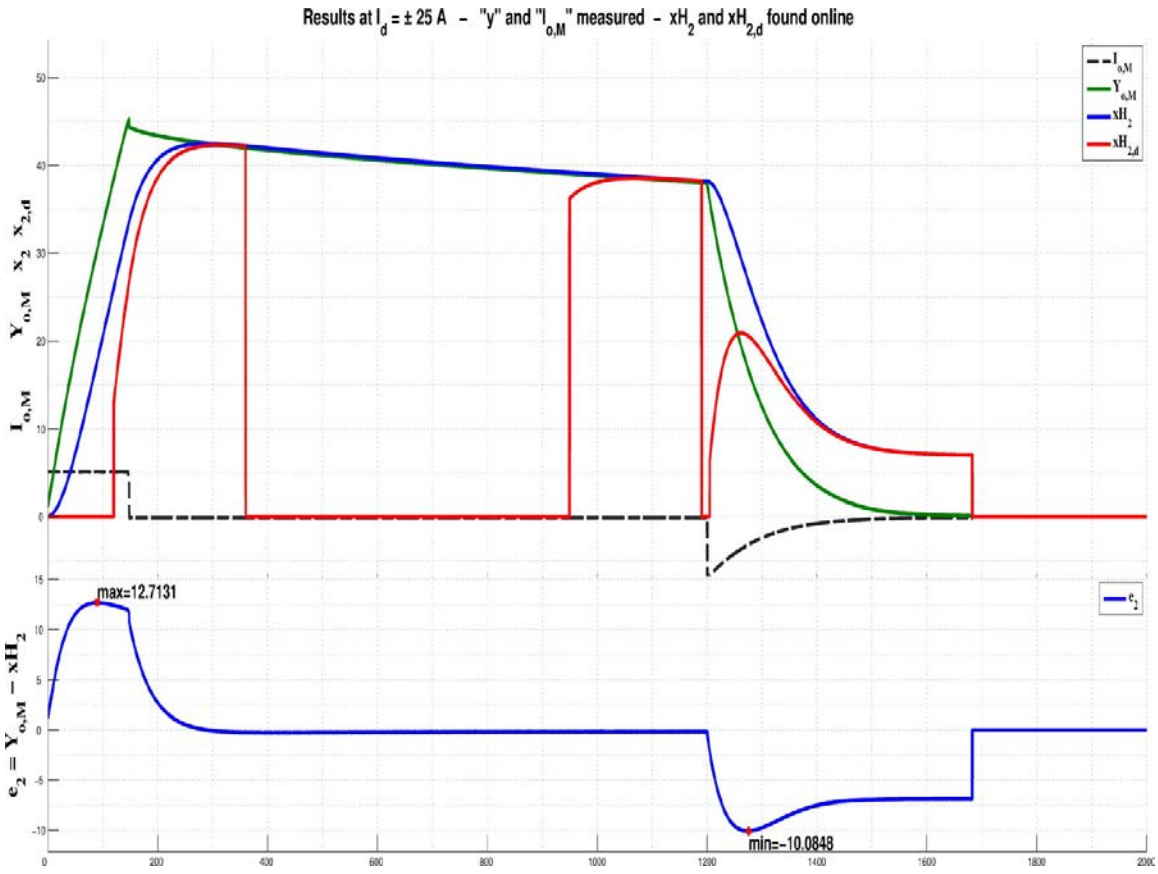

Fig 4.8b – Estimation of $\hat{x}_2$ and $\hat{x}_{2,w}$, with $I_d = \pm 25A$

On top of the figure 4.8b there are the measured current I_o (dotted grey, not in scale; it is useful to point out the 3 phases of: charge $t_0 \sim t_{V_M}$, free discharge $t_{V_M} \sim t_{FE}$, forced discharge $t_{FE} \sim t_f$), the measured voltage y (in green) on SCterminals, the estimated $\hat{x}_2$ by EKF (in blue), the estimated $\hat{x}_{2,w}$ by $wEKF$ (in red). On bottom there is the measure error $e_2 = y - \hat{x}_2$, showing the maximum and minimum values.

Table 4.9 - Numeric results, for $I_d = \pm 30A$

time		I_d	y	$\hat{x}_1$	$\hat{x}_2$
t_0	**0**	**30**	**0.0000**	**0.0000**	**0.0000**
t_{a1}	90	30	36.8561	36.6355	21.5511
t_{y_M}	**114**	**30**	**44.9639**	**44.4017**	**29.5192**
t_{a2}	330	0	42.4224	42.4241	42.5491
t_{b1}	950	0	40.0790	40.0786	40.2209
t_{b2}	1190	0	39.2296	39.2286	39.3690
$t_{V_M} + t_D$	294	0	42.6138	42.6136	42.6011
t_{FE}	**1200**	**-30**	**39.1826**	**39.4022**	**39.3425**
t_{c1}	1210	-30	35.2479	35.4745	39.0152
t_{c2}	1710	-30	0.1007	0.0000	0.0000
$t_{y=2}$	1441	-30	2.0000	2.0965	10.1652
t_F	**2000**	**-30**	**0.0335**	**0.0000**	**0.0000**

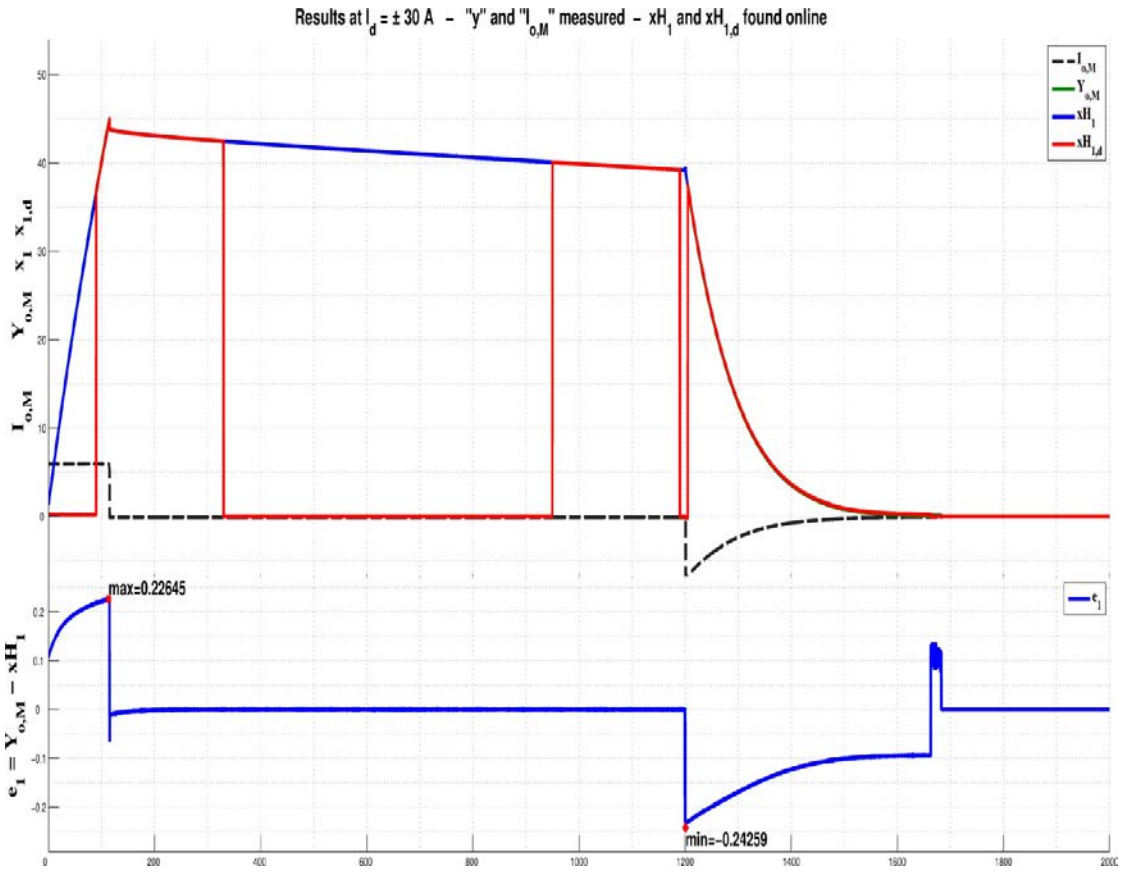

Fig. 4.9a – Estimation of $\hat{x}_1$ and $\hat{x}_{1,w}$, with $I_d = \pm 30A$

On top of the figure 4.9a there are the measured current I_o (dotted grey, not in scale; it is useful to point out the 3 phases of: charge $t_0 \sim t_{V_M}$, free discharge $t_{V_M} \sim t_{FE}$, forced discharge $t_{FE} \sim t_f$), the measured voltage y (in green) on SCterminals, the estimated $\hat{x}_1$ by EKF (in blue), the estimated $\hat{x}_{1,w}$ by $wEKF$ (in red). On bottom there is the measure error $e_1 = y - \hat{x}_1$, showing the maximum and minimum values.

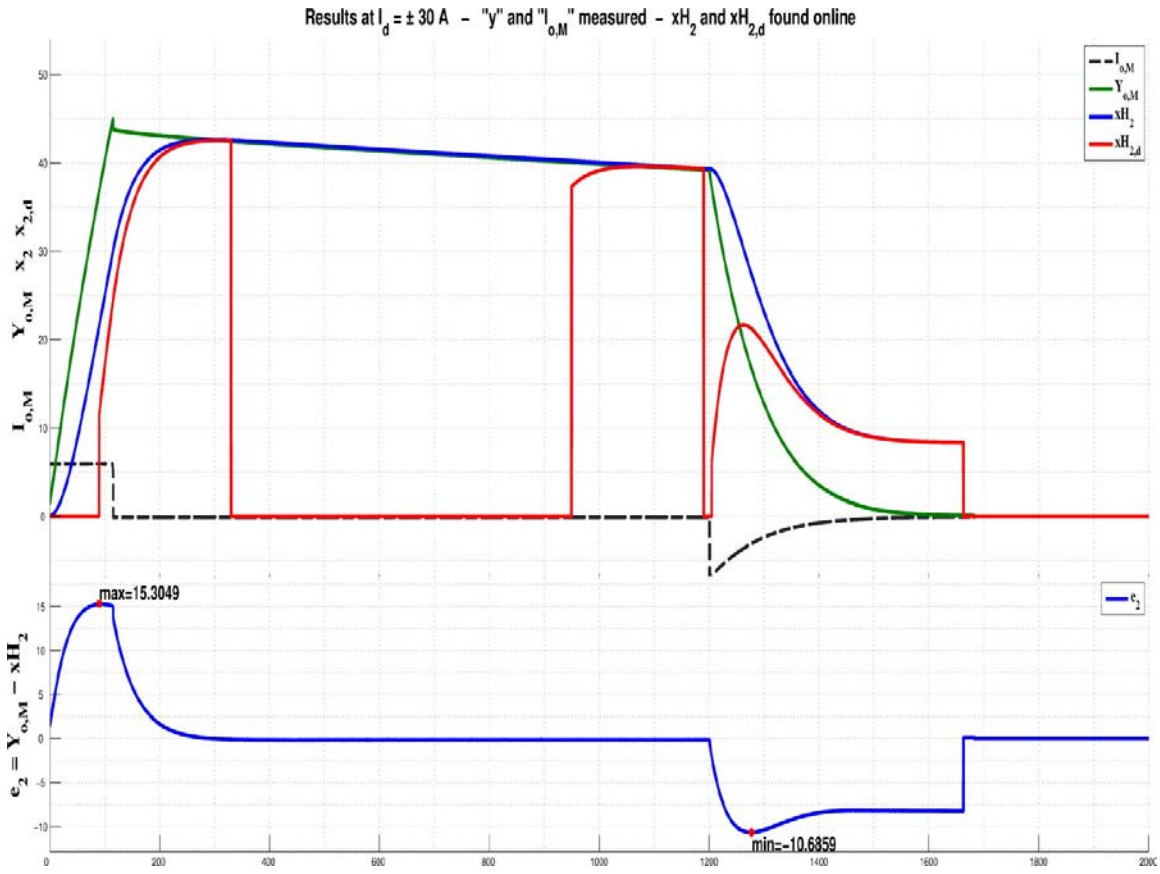

Fig. 4.9b – Estimation of $\hat{x}_2$ and $\hat{x}_{2,w}$, with I_d = ±30*A*

On top of the figure 4.9b there are the measured current I_o (dotted grey, not in scale; it is useful to point out the 3 phases of: charge $t_0 \sim t_{V_M}$, free discharge $t_{V_M} \sim t_{FE}$, forced discharge $t_{FE} \sim t_f$), the measured voltage y (in green) on *SC*terminals, the estimated $\hat{x}_2$ by *EKF* (in blue), the estimated $\hat{x}_{2,w}$ by *wEKF* (in red). On bottom there is the measure error $e_2 = y - \hat{x}_2$, showing the maximum and minimum values.

Table 4.10 - Numeric results, for $I_d = \pm 35A$

time		I_d	y	$\hat{x}_1$	$\hat{x}_2$
t_0	**0**	**35**	**0.0000**	**0.0000**	**0.0000**
t_{a1}	75	35	35.6374	35.3853	18.9595
$t_{ум}$	**101**	**35**	**45.3164**	**44.6745**	**28.6410**
t_{a2}	315	0	42.6541	42.6542	42.8064
t_{b1}	950	0	39.8239	39.8234	39.9766
t_{b2}	1190	0	38.8570	38.8591	39.0452
$t_{V_M} + t_D$	281	0	42.8454	42.8454	42.8970
t_{FE}	**1200**	**−35**	**38.8503**	**39.1045**	**39.0172**
t_{c1}	1210	−35	34.8048	35.0686	38.6995
t_{c2}	1710	−35	0.1141	0.0000	0.0000
$t_{y=2}$	1443	−35	2.0000	2.1214	11.0924
t_F	**2000**	**−35**	**0.0570**	**0.0000**	**0.0000**

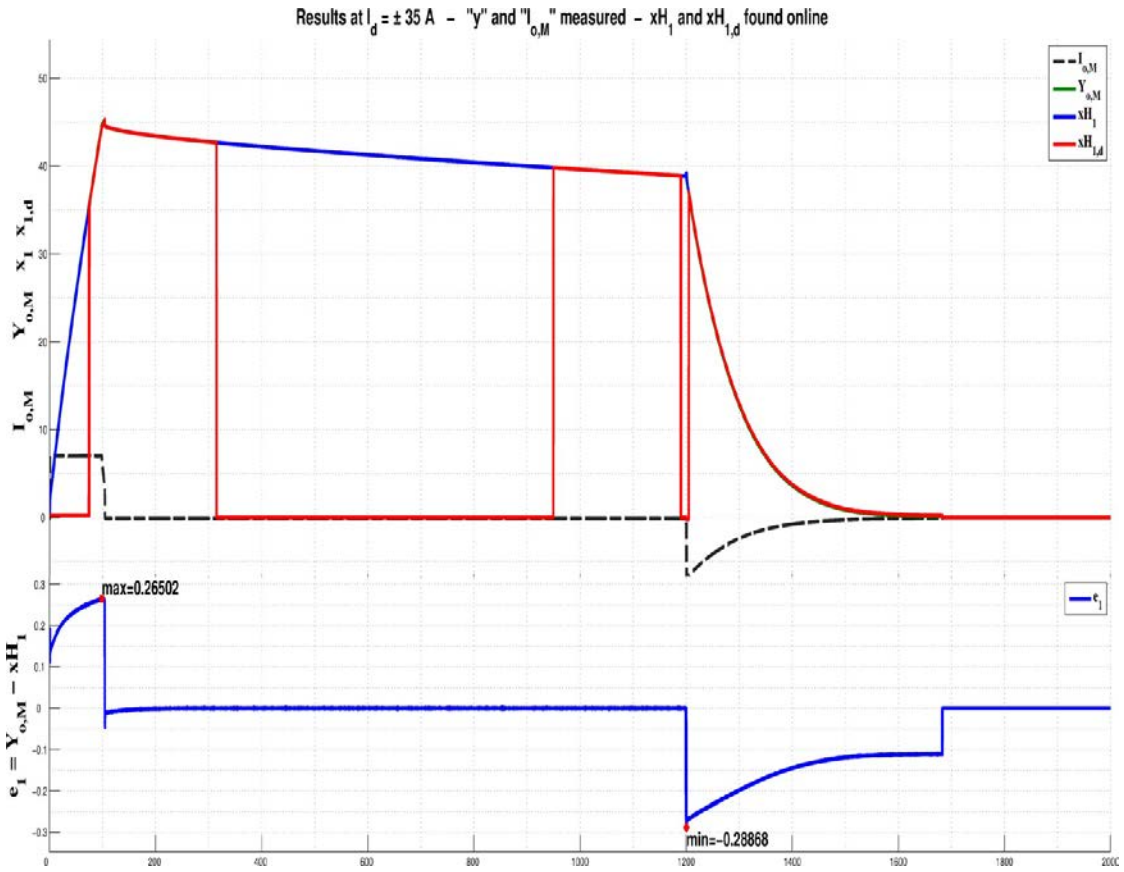

Fig. 4.10a – Estimation of $\hat{x}_1$ and $\hat{x}_{1,w}$, with $I_d = \pm 35A$

On top of the figure 4.10a there are the measured current I_o (dotted grey, not in scale; it is useful to point out the 3 phases of: charge $t_0 \sim t_{V_M}$, free discharge $t_{V_M} \sim t_{FE}$, forced discharge $t_{FE} \sim t_f$), the measured voltage y (in green) on SCterminals, the estimated $\hat{x}_1$ by EKF (in blue), the estimated $\hat{x}_{1,w}$ by $wEKF$ (in red). On bottom there is the measure error $e_1 = y - \hat{x}_1$, showing the maximum and minimum values.

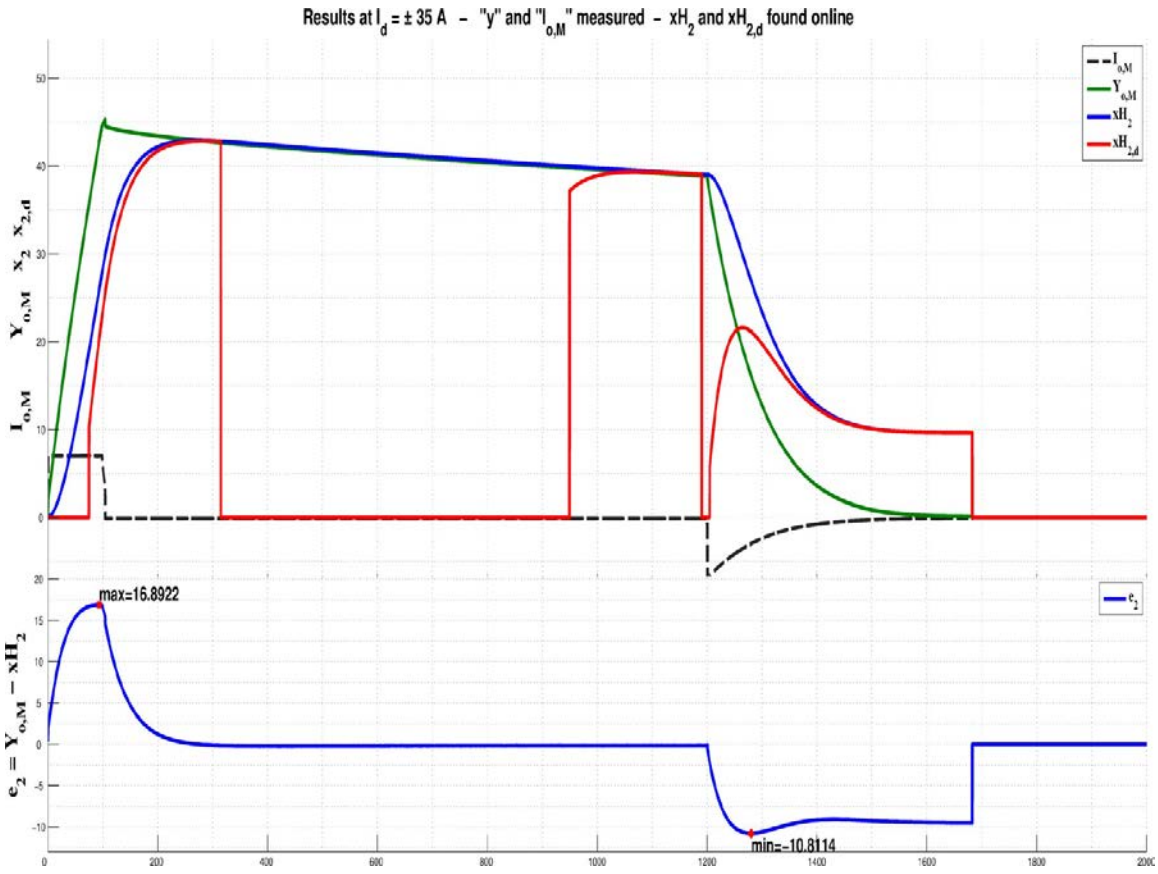

Fig. 4.10b – Estimation of $\hat{x}_2$ and $\hat{x}_{2,w}$, with $I_d = \pm 35A$

On top of the figure 4.10b there are the measured current I_o (dotted grey, not in scale; it is useful to point out the 3 phases of: charge $t_0 \sim t_{V_M}$, free discharge $t_{V_M} \sim t_{FE}$, forced discharge $t_{FE} \sim t_f$), the measured voltage y (in green) on SCterminals, the estimated $\hat{x}_2$ by EKF (in blue), the estimated $\hat{x}_{2,w}$ by $wEKF$ (in red). On bottom there is the measure error $e_2 = y - \hat{x}_2$, showing the maximum and minimum values.

Table 4.11 - Numeric results, for $I_d = \pm 40A$

time		I_d	y	$\hat{x}_1$	$\hat{x}_2$
t_{a1}	70	40	38.3568	38.0623	19.5279
t_{yM}	**83**	**40**	**44.4368**	**43.7585**	**24.9212**
t_{a2}	310	0	41.4287	41.4283	41.5214
t_{b1}	950	0	39.0047	39.0056	39.1706
t_{b2}	1190	0	38.1889	38.1887	38.3214
$t_{V_M} + t_D$	263	0	41.6267	41.6277	41.5590
t_{FE}	**1200**	**−40**	**38.1385**	**38.4296**	**38.2978**
t_{c1}	1210	−40	34.1132	34.4113	38.0234
t_{c2}	1710	−40	0.0906	0.0000	0.0000
$t_{y=2}$	1437	−40	2.0000	2.1243	12.0892
t_F	**2000**	**−5**	**0.0570**	**0.0000**	**0.0000**

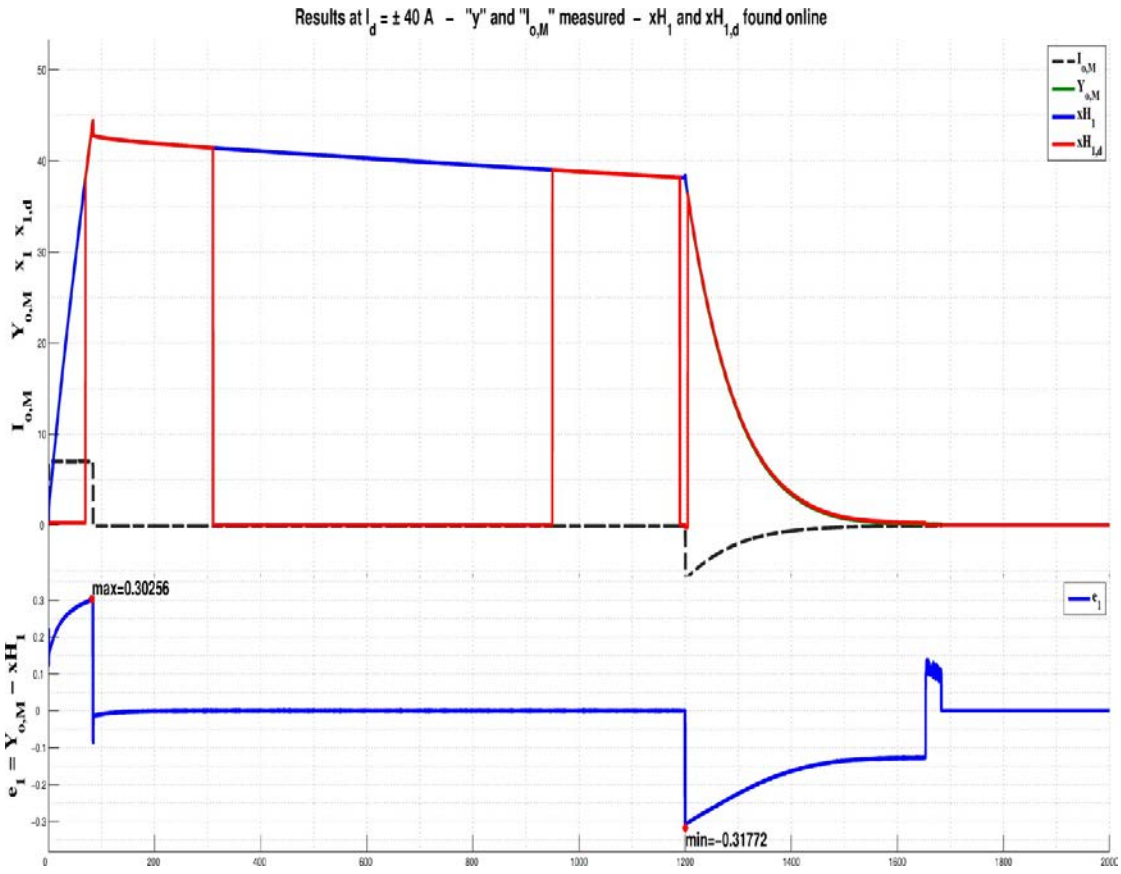

Fig. 4.11a – Estimation of $\hat{x}_1$ and $\hat{x}_{1,w}$, with $I_d = \pm 40A$

On top of the figure 4.11a there are the measured current I_o (dotted grey, not in scale; it is useful to point out the 3 phases of: charge $t_0 \sim t_{V_M}$, free discharge $t_{V_M} \sim t_{FE}$, forced discharge $t_{FE} \sim t_f$), the measured voltage y (in green) on SCterminals, the estimated $\hat{x}_1$ by EKF (in blue), the estimated $\hat{x}_{1,w}$ by $wEKF$ (in red). On bottom there is the measure error $e_1 = y - \hat{x}_1$, showing the maximum and minimum values.

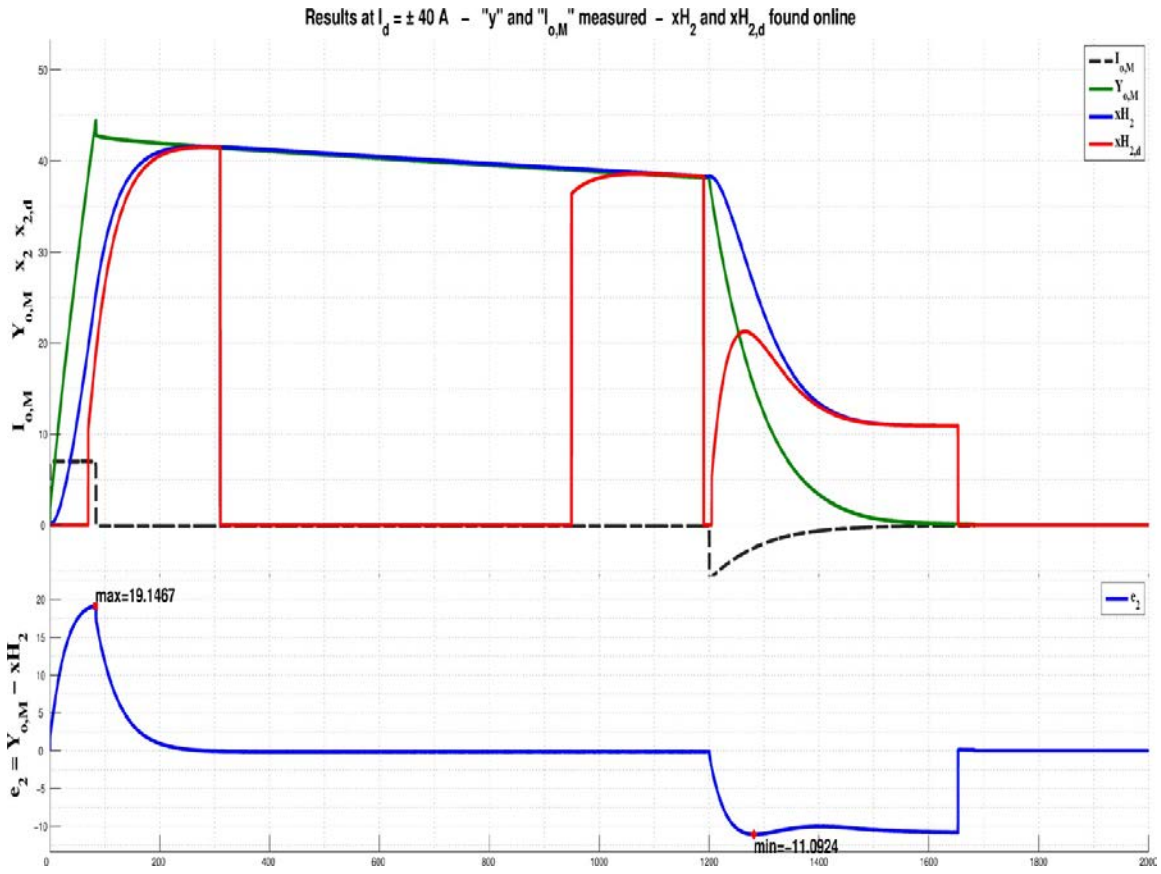

Fig 4.11b – Estimation of $\hat{x}_2$ and $\hat{x}_{2,w}$, with $I_d = \pm 40A$

On top of the figure 4.11b there are the measured current I_o (dotted grey, not in scale; it is useful to point out the 3 phases of: charge $t_0 \sim t_{V_M}$, free discharge $t_{V_M} \sim t_{FE}$, forced discharge $t_{FE} \sim t_f$), the measured voltage y (in green) on SCterminals, the estimated $\hat{x}_2$ by EKF (in blue), the estimated $\hat{x}_{2,w}$ by $wEKF$ (in red). On bottom there is the measure error $e_2 = y - \hat{x}_2$, showing the maximum and minimum values.

4.3 Final remarks

The on-line diagnostic of a supercapacitor is crucial for its reliability, anyway it is a non-linear system since its model contains a capacitance proportional to the voltage. For this reason an extended Kalmal filter is to be designed.

The aim of estimation is to obtain the state variables. They cannot be measured directly since they are decoupled from the voltage at the supercapacitor terminals by the presence of parasitic resistances. For this reason the estimation process must be performed on the basis on the voltage and current at the external terminals.

On this basis both the charge stored in the non-linear capacitance and the parasitic resistance can be evaluated. During normal operation these values are usually constant, if a degradation occurs an increase of the parasitic resistance or a decrease of the stored charge can be appreciated.

The devised extended Kalman filter gives an estimation of both state variables. In particular the voltage at the non-linear capacitance terminals has a very low error hence it can be used for the diagnostic on-line. The error on the voltage at the linear capacitance terminals is relatively higher, anyway it does not jeopardize the diagnostic process since the great part of the supercapacitor charge is stored in the non-linear capacitance expecially at voltage near the rated one in which the supercapacitor is usually operated.

In general the estimation shows the maximum error during transients, on the contrary once the filter is locked no appreciable variation between the real and estimated value is noted. The speed of the convergence is very fast compared to the duration of the transients also in the worst case in which the filter is operated starting from zero initial conditions when the supercapacitor is running.

All results have been verified by simulation and experimentally confirming the goodness of the proposed approach in presence of noise.

Conclusions

This thesis aimed to analyze the supercapacitor behavior to verify the possibility of the estimation of its internal parameters for diagnostic purposes.

The target has been reached firstly by a theoretical analysis which showed that the crucial parameters for diagnostic purposes are the voltage of the non-linear capacitance, since it gives a measure of the stored charge, and the parasitic resistance which limits the maximum allowable current and influences losses.

Secondly it has been verified when a supercapacitor parameters are observable and finally an extended Kalman filter to obtain such parameters has been set up.

The Thesis demonstrated that a supercapacitor can be modelled by a 2-branch Double-Layer capacitor including a non-linear capacitance, it is observable thanks to the fact that such *SC* can be characterized by a parabola in the state space region in which the observability is not guaranteed. It has been shown that this curve usually does not cross the normal operating region corresponding to a part of the first quadrant of the state space plane.

Then the internal parameters have been estimated by an *Extended Kalman Filter*, or *EKF*. A windowed-*EKF*, or *wEKF*, has been used for

learning the *EKF* behavior, when it has to engage with measured the output *y* with respect to pre-configured time ranges. The main parameter to be estimated has been identified in the voltage of the non-linear capacitance since it gives a measure of the stored charge and of the parasitic resistance.

The goal of diagnostics is reached since a very low error between the real and estimated values of the voltage on the non-linear capacitance has been obtained.

The assessed method can be operated on-line: during the lifecycle of a *SC*, some values could differ from rated ones; so that, a possible *SC* degradation can be detected. In this case the *SC* replacement can be programmed with benefits for operators and equipment.

References

[1] R. Faranda, “A new parameters identification procedure for simplified double layer capacitor two-branch model,” *Electric Power Systems Research*, vol. 80, no. 4, pp. 363–371, 2010.

[2] M. Pucci, G. Vitale, G. Cirrincione, and M. Cirrincione, “Parameter identification of a double-layer-capacitor 2-branch model by a least- squares method,” in *Industrial Electronics Society, IECON 2013-39th Annual Conference of the IEEE*. IEEE, 2013, pp. 6770–6776.

[3] D. V. Ragone, “Review of battery systems for electrically powered vehicles,” SAE Technical Paper, Tech. Rep., 1968.

[4] J. Both, “Electrolytic capacitors, 1890 to 1925: early history and basic principle,” *Electrical Insulation Magazine, IEEE*, vol. 31, no. 1, pp. 22–29, 2015.

[5] D. Linden and T. B. Reddy, “Handbook of batteries 3rd,” 2002.

[6] R. Khurmi and R. Sedha, *Materials Science*. S. Chand, 2008.

[7] N. Karim and S. Jonathan, “How fuel cells work: Polymer exchange membrane fuel cells,” *How Stuff Works, accessed August*, vol. 4, 2011.

[8] E. Spila, S. Panero, and B. Scrosati, “Condensatori elettrochimici ad alta capacità,” *La Chimica e l’industria*, vol. 77, no. 6, pp. 333–340, 1995.

[9] H. Gualous, H. Louahlia, and R. Gallay, "Supercapacitor characterization and thermal modelling with reversible and irreversible heat effect," *Power Electronics, IEEE Transactions on*, vol. 26, no. 11, pp. 3402–3409, 2011.

[10] F. Belhachem, S. Rael, and B. Davat, "A physical based model of power electric double-layer supercapacitors," in *Industry Applications Conference, 2000. Conference Record of the 2000 IEEE*, vol. 5. IEEE, 2000, pp. 3069–3076.

[11] M. Rose and S. Merryman, "Electrochemical capacitor technology for actuator applications," in *Energy Conversion Engineering Conference, 1996. IECEC 96., Proceedings of the 31st Intersociety*, vol. 1. IEEE, 1996, pp. 245–250.

[12] B. E. Conway, *Electrochemical supercapacitors: scientific fundamentals and technological applications*. Springer Science & Business Media, 2013.

[13] M. S. Halper and J. C. Ellenbogen, "Supercapacitors: A brief overview,"*The MITRE Corporation, McLean, Virginia, USA*, pp. 1–34, 2006.

[14] A. M. Namisnyk, "A survey of electrochemical supercapacitor technology," Ph.D. dissertation, University of Technology, Sydney, 2003.

[15] Panasonics, *Gold Capacitor Technical Guide*, 2005.

[16] X. Jiang, J. Polastre, and D. Culler, "Perpetual environmentally powered sensor networks," in *Information Processing in Sensor Networks, 2005. IPSN 2005. Fourth International Symposium on*. IEEE, 2005, pp. 463– 468.

[17] S. Buller, E. Karden, D. Kok, and R. De Doncker, "Modeling the dynamic behavior of supercapacitors using impedance spectroscopy," in *Industry Applications Conference, 2001. Thirty-Sixth IAS Annual Meeting. Conference Record of the 2001 IEEE*, vol. 4. IEEE, 2001, pp. 2500–2504.

[18] L. Zubieta and R. Bonert, "Characterization of double-layer capacitors for power electronics applications," *Industry Applications, IEEE Transactions on*, vol. 36, no. 1, pp. 199–205, 2000.

[19] A. S. Weddell, G. V. Merrett, T. J. Kazmierski, and B. M. Al-Hashimi, "Accurate supercapacitor modeling for energy harvesting wireless sensor nodes," *Circuits and Systems II: Express Briefs, IEEE Transactions on*, vol. 58, no. 12, pp. 911–915, 2011.

[20] M. S. Islam, M. B. Hossain, M. N. Hossain, S. B. Alam, M. Enamul, and H. Chowdhury, "Modeling of a double-layer capacitor with individual branch response," in *Proceedings of the World Congress on Engineering and Computer Science*, vol. 2. Citeseer, 2010.

[21] Z. Yicheng, L. Haiquan, X. Haitao, and W. Lulu, "Analysis of the time- domain and frequency-domain models of supercapacitors," in *Vehicle Power and Propulsion Conference, 2008. VPPC'08. IEEE*. IEEE, 2008, pp. 1–4.

[22] F. Alonge, M. Cirrincione, G. Vitale, and G. Rodonò, "Observability of a 2-branch double-layer-capacitor," *ISSN 2172-038 X, April 2015*, no. 13, p. 7, 2015.